Extreme Mechanics Letters 40 (2020) 100977

Contents lists available at ScienceDirect

Extreme Mechanics Letters

journal homepage: www.elsevier.com/locate/eml

Design of tunable acoustic metamaterials with periodic piezoelectric microstructure

Andrea Bacigalupo [a], Maria Laura De Bellis [b], Diego Misseroni [c,*]

[a] University of Genoa, Department DICCA, via Montallegro 1, Genoa, Italy
[b] University of Chieti-Pescara, Department INGEO, Viale Pindaro 42, Pescara, Italy
[c] University of Trento, via Mesiano 77, Trento, Italy

ARTICLE INFO

Article history:
Received 7 June 2020
Received in revised form 3 August 2020
Accepted 8 September 2020
Available online 14 September 2020

Keywords:
Periodic microstructure
Piezoelectric shunting
Tunable metamaterials
Bloch wave propagation
Band gap control

ABSTRACT

An innovative special class of tunable periodic metamaterials is designed, suitable for realizing high-performance acoustic filters. The metamaterial is made up of a phononic crystal coupled to local resonators. Such local resonators consist of masses enclosed into piezoelectric rings, shunted by either dissipative or non-dissipative electrical circuit. By tuning the impedance/admittance of such electrical circuits, it is possible to fully adjust the constitutive properties of the shunting piezoelectric material. This feature paves the way for unconventional behaviours, well beyond the capabilities achievable with classical materials. It follows that the acoustic properties of the periodic metamaterial can be adaptively modified, in turn, opening new possibilities for the control of pass and stop bands. By exploiting a generalization of the Floquet–Bloch theory, the in-plane free wave propagation in the tunable metamaterial is investigated, by varying a certain tuning parameter, to show the efficiency of the proposed shunting piezoelectric system as a wave propagation control device. Particular attention is devoted to the determination of the in-plane constitutive equations of the shunting piezoelectric phase in the transformed Laplace space. Finally, broad design directions of tunable acoustic filters aiming to a changing performance requirement in real-time, is also provided.

1. Introduction

The study of metamaterials is increasingly emerging as a cutting edge interdisciplinary area, including physics, material science and engineering. Metamaterials are engineered composites, specifically tailored to exhibit outstanding constitutive properties, well above those achievable with classical materials. First introduced in optics and photonics [1,2], metamaterials have afterwards established themselves in the fields of elastodynamics and acoustics [3–5] for a wide range of intriguing applications ranging from filtering, to wave-guiding, self-collimation, mechanical energy transfer, wave polarization up to band-gaps control, i.e. more generally manipulation of the dispersive properties of vibrational waves [6–27]. By focusing on this latter context, acoustic metamaterials have being designed from periodic distributions of inclusions (or scatterers) embedded in a matrix, i.e. phononic crystals, with the addition of local resonators which enable unique sub-wavelength properties to emerge accordingly with Lu et al. [28], Liu et al. [29]. The core idea behind their design is to engineer the architecture and the geometry of their microstructure at different scales of interest in order to achieve unusual macroscopic properties. In order to meet the requirement of optimal design, parametric and topological optimization techniques can be successfully used [30–38]. Within the framework of acoustic metamaterials, some of the limitations of standard materials such as negative refraction [22,39–42], superlenses [43–45], and invisibility of defects embedded into both lattice and continuous systems [46–50] can be overcome. These astonishing features, unachievable with natural materials, have found application in the fabrication of new devices such as concentration detectors, vibration dampers and also in the protection of buildings from earthquakes [51–60]. Different techniques have been proposed to accomplish the aforementioned targets. Some of these include the change of the mechanical properties of the material, such as mass density, inertia and stiffness [48,61–65], others the insertion of spatially-local inertial or Helmholtz resonators within either lattice materials or microstructured continuum materials [66–74].

More sophisticated techniques are based on the use of active phases exploiting multi-field couplings, such as the electro- or the magneto-mechanical one, to achieve the wave propagation control. These approaches leave wide freedom of design without changing the mass of the system. In particular, the pioneering work of Forward [75] demonstrated the efficiency of piezoelectric elements connected to electrical circuits for vibration control. More specifically, one way to couple the mechanical and the electrical fields concerns the use of piezoelectric patches shunted

* Corresponding author.
E-mail address: diego.misseroni@unitn.it (D. Misseroni).

https://doi.org/10.1016/j.eml.2020.100977
2352-4316/

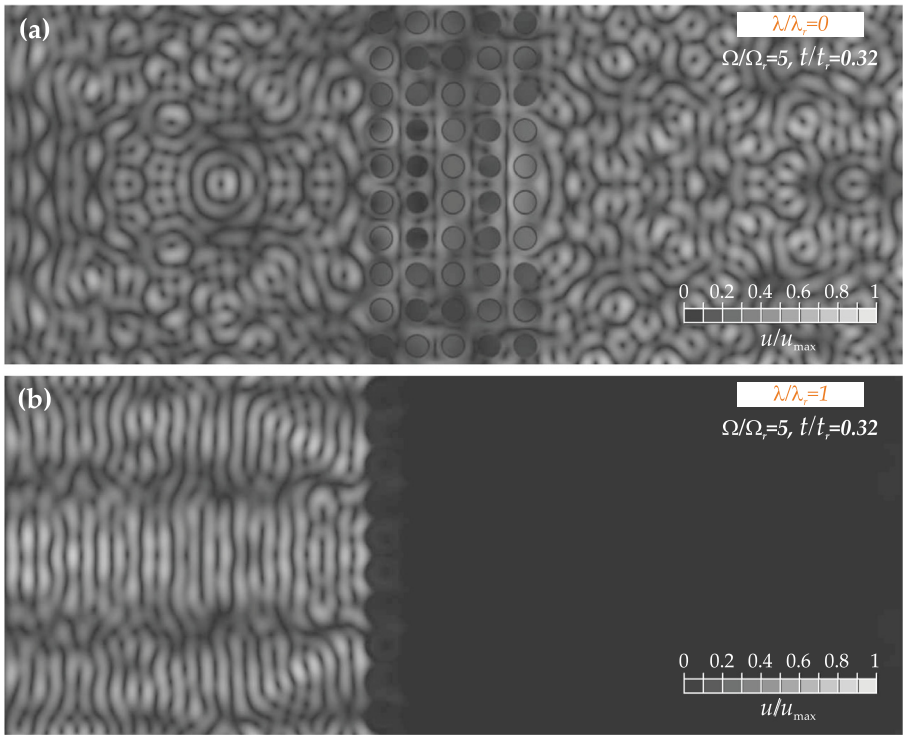

Fig. 1. Filtering performance of the tunable metamaterials. A rectangular strip of homogeneous material, with a central core made by a portion of the metamaterial, undergoes a mono-frequency time-harmonic displacement excitation. (a) case of excitation frequency falling into a pass band; (b) case of excitation frequency falling into a stop band.

by electrical networks (*shunted piezoelectric phases*) in both active and passive control schemes. Contrary to active control, in passive schemes, a sensing element is not necessary. In most cases, the metastructure consists of an array of passive electrical circuits mounted on the vibrating structure, each of them directly connected to the piezoelectric device [76–83]. A detailed review of different shunt piezoelectric systems for noise, vibration and wave propagation control is provided in [84–86]. The case of metamaterials with piezoelectric phases shunted by dissipative and/or non-dissipative electrical circuit, characterized by variable capacitors, is widely investigated in the spectral design of waveguides and/or acoustic filters [87–97].

Within this context, in the present paper the constitutive properties of a tunable metamaterial, made of a piezoelectric phase coupled to a generic electrical circuit with a certain equivalent admittance, are consistently determined both in the physical space and in the frequency transformed space. More specifically, in the case of generic dissipative electrical circuits the constitutive relations are in general frequency-dependent. On the other hand, with regard to non-dissipative electrical circuits, when they are characterized by (i) purely capacitive equivalent admittance, frequency-independent constitutive relations are obtained; (ii) purely inductive equivalent admittance, frequency-dependent constitutive relations are obtained.

In particular, with the aim of designing high-performance tunable acoustic filters for the passive wave propagation control, a specific class of periodic metamaterials with a phase shunted by either a dissipative or non dissipative electrical circuit is here proposed. The three phase metamaterial is characterized by a phononic crystal coupled to local resonators. The phononic crystal is made by an in-plane periodic tessellation of rigid and heavy external rings enclosed within a soft and light matrix, while the local resonators consist of rigid and heavy internal disks connected to the external rings through inner rings made of a piezoelectric material shunted by an electrical circuit. The main idea is to properly modifying the equivalent impedance/admittance of the electrical circuit in order to tune the constitutive properties of the shunting piezoelectric phase. This means that, within the design of the metamaterial, its overall constitutive properties can be fully tailored by adjusting parameters of the electrical circuit, without modifications of the microstructural geometry and/or of the non shunted material properties. As a consequence, a control of the band structure of the periodic metamaterial is performed, in terms of amplitude and central frequency of pass and stop bands. More specifically, focus is on a non dissipative electrical circuit, i.e. an adaptive capacitor with both positive and negative capacitance, leading to a real-valued Floquet–Bloch spectrum. A critical investigation of the metamaterial behaviour, as a set of design geometric parameters change, is useful to provide broad guidelines to achieve optimal design solutions.

In order to test the effectiveness of the periodic tunable metamaterial as acoustic filter, a numerical experiment has been performed on a thin rectangular strip of homogeneous material in which a central strip has been replaced by a portion of the metamaterial reported in Fig. 1. A mono-frequency time-harmonic displacement excitation is imposed on the left side of the specimen. By properly tuning the parameters characterizing the electrical circuit, the frequency band-structure is modified. In the case the excitation frequency falls into a pass band no filtering properties are exhibited as in Fig. 1(a), where it emerges that the wave front passes through the microstructured core without significant reduction in the vibration amplitude. On the other hand, when the excitation frequency falls into a stop band, the tunable metamaterial behaves as a highly efficient acoustic filter as in Fig. 1(b), in which the wave front is nearly entirely reflected and trapped in the microstructured core.

The paper is organized as follows. In Section 2 the periodic material with a piezoelectric phase shunted by an electrical circuit is described. In Section 2.1 the in-plane constitutive equations of the orthotropic shunted piezoelectric phase are derived both

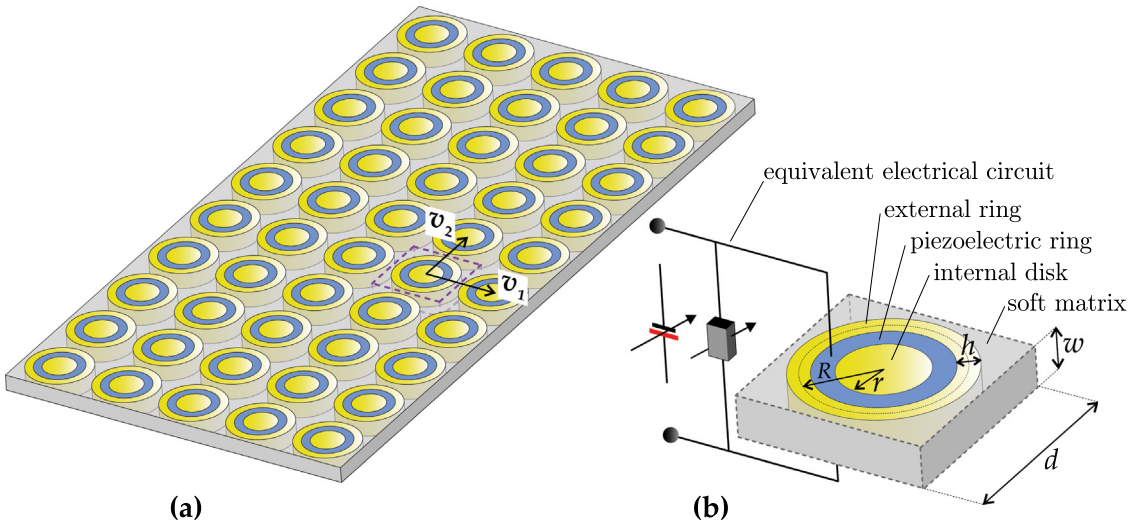

Fig. 2. (a) A generic portion of the heterogeneous material; (b) Scheme of the Periodic Cell containing the shunted piezoelectric material.

for either an electrical circuit characterized by generic equivalent admittance or for one characterized by purely capacitive equivalent admittance. Section 2.2 is devoted to the dynamic governing equations of the periodic material with a shunted piezoelectric phase. Within the framework of a first-order continuum, the governing equation of the in-plane free Bloch wave propagation together with the Floquet–Bloch boundary conditions, imposed on the periodic cell, are defined. In Section 3.1 numerical experiments are devoted to demonstrate the effectiveness of the pass and stop bands tunable control of the proposed shunted metamaterial. Section 3.2 focuses on the performance as a filter of the designed tunable metamaterial in the framework of a numerical experiment. Finally, some concluding remarks are summarized in Section 4. For the convenience of the readers a comprehensive list of the symbols introduced in the article is reported in Table 1.

2. Tunable metamaterials with piezoelectric shunting

We focus on an infinite periodic three-phase microstructured metamaterial, a generic portion of which is schematically depicted in Fig. 2(a).

Such periodic material is characterized by the in-plane regular repetition of a periodic cell, see Fig. 2(b), along two orthogonal periodicity vectors $\mathbf{v}_1 = d\mathbf{e}_1$, $\mathbf{v}_2 = d\mathbf{e}_2$, with $\mathbf{e}_1$ and $\mathbf{e}_2$ being a given orthogonal base. The periodic cell $\mathfrak{A}$, of thickness w, is made of an external soft and light matrix embedding both an outer rigid and heavy ring (with mean radius R) and an inner ring made of a shunted piezoelectric material of thickness h. The geometry is completed by a circular disk, of radius r, made of the same material as the outer ring. In this configuration each piezoelectric ring is connected in parallel through electrodes to an external electrical circuit with tunable equivalent impedance/admittance, see Fig. 2(b). In this framework, the constitutive properties of the piezoelectric shunting can be modified by varying such equivalent impedance/admittance to control the spectral properties of the acoustic metamaterial. In this way the stop- and pass-band frequency can be properly shifted in order to filter Bloch waves propagating in the material at a given frequency.

In the following we will focus first on the treatment of the constitutive properties that characterize the piezoelectric shunting phase (Section 2.1). Then the field equations governing the dynamic behaviour of the metamaterial will be introduced, consistently with the constitutive equations of both the shunted piezoelectric phase and the other characterized by linear elastic behaviour (Section 2.2).

2.1. Shunted piezoelectric constitutive model

We aim to define the time-dependent in-plane constitutive equations governing the shunting piezoelectric phase. In this regard, we start from a three-dimensional orthotropic piezoelectric material with polarization along the $\mathbf{e}_3 = \mathbf{e}_1 \times \mathbf{e}_2$ unit vector, according with the pioneering work by Hagood and von Flotow [76], where each material point is identified by its position vector $\mathbf{x} = x_i\mathbf{e}_i$, with $i = 1, 2, 3$, referred to a coordinate system with origin at point O at time t. The corresponding coupled constitutive relations together with the related ones in the transformed Laplace space are detailed in Appendix A. After proper manipulations, the constitutive relations expressed in terms of the transformed electric potential difference $\widehat{V}_3$, imposed between the two opposite external surfaces of the piezoelectric ring orthogonal to $\mathbf{e}_3$, and the transformed current $\widehat{I}_3$ along the $\mathbf{e}_3$ direction are defined in the Laplace domain, become

$$
\begin{aligned}
&\widehat{\sigma}_{ij} = C_{ijhk}\,\widehat{\varepsilon}_{hk} + C_{ij33}\,\widehat{\varepsilon}_{33} - \frac{e_{ij3}\widehat{V}_3}{L^{(P)}},\\
&\widehat{\sigma}_{33} = C_{33hk}\,\widehat{\varepsilon}_{hk} + C_{3333}\,\widehat{\varepsilon}_{33} - \frac{e_{333}\widehat{V}_3}{L^{(P)}},\\
&\widehat{\sigma}_{\alpha 3} = 2\,C_{\alpha 3\alpha 3}\,\widehat{\varepsilon}_{\alpha 3} + e_{\alpha 3\alpha}\,\frac{\partial\widehat{\phi}}{\partial x_\alpha},\\
&\widehat{D}_i = 2\,\widetilde{e}_{ij3}\,\widehat{\varepsilon}_{j3} + \beta_{ij}\,\frac{\partial\widehat{\phi}}{\partial x_j},\\
&\widehat{I}_3 = s\,A^{(P)}\widetilde{e}_{3jh}\,\widehat{\varepsilon}_{jh} + s\,A^{(P)}\widetilde{e}_{333}\,\widehat{\varepsilon}_{33} + Y_{33}^{(P)}(s)\,\widehat{V}_3,\\
&\qquad i, j, h, k, \alpha = 1, 2,
\end{aligned}
\tag{1}
$$

where from now on no summation on index α is applied, and being $\widehat{\sigma}_{pq}$ the components of the transformed stress tensor, $\widehat{D}_p$ the components of the transformed electric displacement field, $\widehat{\varepsilon}_{rs} = (\partial\widehat{u}_r/\partial x_s + \partial\widehat{u}_s/\partial x_r)/2$ is the components of the transformed strain tensor, with $\widehat{u}_p$ the transformed displacement field components, $\widehat{\phi}$ the transformed electric potential field, C_{pqrs} the components of the fourth order elasticity tensor, β_{pr} the components of the second order dielectric permittivity tensor, e_{qsp} the components of the third order piezoelectric stress–charge coupling tensor and its transpose $\widetilde{e}_{pqs} = e_{qsp}$. Moreover, the auxiliary variable $Y_{33}^{(P)}(s) = \left(sA^{(P)}/L^{(P)}\right)\beta_{33}$ has been introduced, playing the role of the admittance of the piezoelectric material in the $\mathbf{e}_3$ direction, being $A^{(P)} = \pi((R - h/2)^2 - r^2)$ the area of the piezoelectric annulus, and $L^{(P)} = w$.

Table 1
List of symbols.

Symbol	Explanation	Symbol	Explanation
$\mathcal{L}$	Bilateral Laplace transform operator	$\mathbf{m}$	Outward normal unit vector
$\mathcal{L}^{-1}$	Inverse bilateral Laplace transform operator	Γ	Closed polygonal curve
$\mathcal{F}^{-1}$	Inverse Fourier transform operator	Ξ	Curvilinear abscissa
$*$	Convolution product	Ξ_j	Vertices of Γ
$\mathbf{e}_j$	jth unit vector of the canonical basis	t	Temporal variable
ι	Imaginary unit	s	Complex angular frequency
δ	Dirac delta function	ω	Angular frequency
$\mathfrak{A}$	Periodic cell	R, r, h, w	Geometric dimensions of the microstructure
$\partial\mathfrak{A}$	Boundary of $\mathfrak{A}$	u_j	displacement field component
$\partial\mathfrak{A}^{\pm}$	Positive/negative part of $\partial\mathfrak{A}$	ε_{ij}	Strain tensor component
d	Edge of the periodic cell	ϕ	electric potential field
$\mathbf{v}_j$	jth periodicity vector	σ_{ij}	Stress tensor component
$\mathbf{x}$	Position vector	D_j	electric displacement component
$\mathbf{x}^{\pm}$	Position vector of the point $P \in \partial\mathfrak{A}^{\pm}$	V_3	Electric potential difference in $\mathbf{e}_3$
x_j	component of $\mathbf{x}$	I_3	Current in $\mathbf{e}_3$
$\mathfrak{B}$	Dimensionless first Brillouin zone	C_{ijhk}	Elasticity tensor component
$\mathbf{k}$	Wave vector	β_{ij}	Dielectric permittivity tensor component
k_j	component of $\mathbf{k}$	e_{ijk}, $\widetilde{e}_{ijk}$	stress–charge coupling tensor component
ρ	Mass density	$\bar{g}$	Laplace transformed function of g
$\bar{g}^{\pm}$	Value of $\bar{g}$ in $\mathbf{x}^{\pm}$	$\widehat{b}_j$	component of the transformed source term
$A^{(P)}$	Area of the piezoelectric annulus	$L^{(P)}$	Dimension of the piezoelectric phase in $\mathbf{e}_3$
$Y_{33}^{(EL)}$	Total equivalent admittance	$Y_{33}^{(P)}$	Equivalent admittance of the piezoelectric material
$Y_{33}^{(SU)}$	Equivalent shunting admittance	$Z_{33}^{(EL)}$	Total equivalent impedance
$\lambda(s)$	Tuning function	λ	Tuning parameter
λ_R	Resonance value of the tuning parameter	λ^*	Shifted tuning parameter
$\mathcal{C}$	Capacitance	C_{ijhk}^{EL}	Equivalent elastic tensor component of the shunted piezoelectric phase
β_{ij}^{EL}	Equivalent dielectric permittivity tensor component of the shunted piezoelectric phase	C_{ijhk}^{EL0}	Value of C_{ijhk}^{EL} for $\lambda = 0$
$C_{ijhk}^{EL\infty}$	Value of C_{ijhk}^{EL} for $\lambda \to \pm\infty$	$C_{ijkl}^{\diamond}$	Equivalent elastic tensor component of the tunable metamaterial

In the case of shunting piezoelectric material, in which an electrical circuit is connected in parallel to the piezoelectric ring, see Fig. 2(b), the equivalent shunting admittance $Y_{33}^{(SU)}$ sums to the piezoelectric one $Y_{33}^{(P)}$. Details concerning the constitutive relations of the electrical circuit in terms of transformed electric potential difference $\widehat{V}_3$ and of the transformed current $\widehat{I}_3$ are discussed in Appendix B. In agreement with this assumption, the last equation of (1) specializes into

$$\widehat{I}_3 = sA^{(P)}\widetilde{e}_{3jh}\,\widehat{\varepsilon}_{jh} + sA^{(P)}\widetilde{e}_{333}\,\widehat{\varepsilon}_{33} + Y_{33}^{(EL)}(s)\,\widehat{V}_3, \qquad j,h = 1,2, \quad (2)$$

being $Y_{33}^{(EL)}(s) = Y_{33}^{(P)}(s) + Y_{33}^{(SU)}(s)$ the total equivalent admittance. It is worth-noting that in the general case the constitutive variable $Y_{33}^{(EL)}$ explicitly depends on the complex Laplace variable s.

After proper manipulations of Eq. (2), the electric potential difference $\widehat{V}_3$ is made explicit and can be plugged into (1), so that

$$\widehat{\sigma}_{33} = \left(C_{33hk} + e_{333}\frac{sA^{(P)}}{L^{(P)}}Z_{33}^{(EL)}(s)\widetilde{e}_{3hk}\right)\widehat{\varepsilon}_{hk} + \\ + \left(C_{3333} + e_{333}\frac{sA^{(P)}}{L^{(P)}}Z_{33}^{(EL)}(s)\widetilde{e}_{333}\right)\widehat{\varepsilon}_{33} - \frac{e_{333}Z_{33}^{(EL)}(s)}{L^{(P)}}\widehat{I}_3, \quad (3)$$

where the total equivalent impedance $Z_{33}^{(EL)}(s) = 1/Y_{33}^{(EL)}(s)$ is introduced. Moreover, the strain component $\widehat{\varepsilon}_{33}$ can be made explicit in Eq. (3) and plugged, in turn, into Eq. (1), therefore the following in-plane relations are obtained

$$\widehat{\sigma}_{ij} = \left[C_{ijhk} + e_{ij3}\frac{sA^{(P)}}{L^{(P)}}Z_{33}^{(EL)}(s)\widetilde{e}_{3hk} - \left(C_{ij33} + e_{ij3}\frac{sA^{(P)}}{L^{(P)}}Z_{33}^{(EL)}(s)\widetilde{e}_{333}\right)\times \right. \\ \left. \times\frac{C_{33hk} + e_{333}\frac{sA^{(P)}}{L^{(P)}}Z_{33}^{(EL)}(s)\widetilde{e}_{3hk}}{C_{3333} + e_{333}\frac{sA^{(P)}}{L^{(P)}}Z_{33}^{(EL)}(s)\widetilde{e}_{333}}\right]\widehat{\varepsilon}_{hk} + \\ - \left[\frac{e_{ij3}Z_{33}^{(EL)}(s)}{L^{(P)}} - \left(C_{ij33} + e_{ij3}\frac{sA^{(P)}}{L^{(P)}}Z_{33}^{(EL)}(s)\widetilde{e}_{333}\right)\times \right. \\ \left. \times\frac{\frac{e_{333}Z_{33}^{(EL)}(s)}{L^{(P)}}}{C_{3333} + e_{333}\frac{sA^{(P)}}{L^{(P)}}Z_{33}^{(EL)}(s)\widetilde{e}_{333}}\right]\widehat{I}_3 + \\ + \frac{C_{ij33} + e_{ij3}\frac{sA^{(P)}}{L^{(P)}}Z_{33}^{(EL)}(s)\widetilde{e}_{333}}{C_{3333} + e_{333}\frac{sA^{(P)}}{L^{(P)}}Z_{33}^{(EL)}(s)\widetilde{e}_{333}}\bar{\sigma}_{33},$$

$$\widehat{D}_\alpha = \frac{\widetilde{e}_{\alpha\alpha3}}{C_{\alpha3\alpha3}}\bar{\sigma}_{\alpha3} - \left(\beta_{\alpha\alpha} + \frac{e_{\alpha3\alpha}\widetilde{e}_{\alpha\alpha3}}{C_{\alpha3\alpha3}}\right)\frac{\partial\widehat{\phi}}{\partial x_\alpha}, \qquad i,j,h,k,\alpha = 1,2. \quad (4)$$

For the sake of convenience, the total equivalent admittance of the shunting piezoelectric material can be expressed as $Y_{33}^{(EL)}(s) = sA^{(P)}\beta_{33}^{EL}(s)/L^{(P)}$, where the auxiliary s-dependent function $\beta_{33}^{EL}(s) = \beta_{33}[1 + L^{(P)}Y_{33}^{(SU)}(s)/(s\,\beta_{33}A^{(P)})] = \beta_{33}\,(1 + \lambda(s))$ is introduced, with the so-called *tuning function* $\lambda(s) = L^{(P)}Y_{33}^{SU}(s)/(s\,\beta_{33}A^{(P)})$ linearly depending on the generic equivalent shunting admittance $Y_{33}^{(SU)}(s)$ that, in turn, may depend on one or more tuning parameters characterizing the specific electrical circuit.

Focusing on the particular case characterized by $\widehat{I}_3 = 0$, $\bar{\sigma}_{i3} = 0$ with $i = 1, 2, 3$, the in-plane constitutive relations (4) become

$$\widehat{\sigma}_{ij} = \left[C_{ijhk} + \frac{e_{ij3}\widetilde{e}_{3hk}}{\beta_{33}^{EL}(\lambda(s))} + \right. \\ \left. - \left(C_{ij33} + \frac{e_{ij3}\widetilde{e}_{333}}{\beta_{33}^{EL}(\lambda(s))}\right)\left(\frac{C_{33hk} + \frac{e_{333}\widetilde{e}_{3hk}}{\beta_{33}^{EL}(\lambda(s))}}{C_{3333} + \frac{e_{333}\widetilde{e}_{333}}{\beta_{33}^{EL}(\lambda(s))}}\right)\right]\widehat{\varepsilon}_{hk},$$

$$\widehat{D}_\alpha = -\left(\beta_{\alpha\alpha} + \frac{e_{\alpha3\alpha}\widetilde{e}_{\alpha\alpha3}}{C_{\alpha3\alpha3}}\right)\frac{\partial\widehat{\phi}}{\partial x_\alpha}, \qquad i,j,h,k,\alpha = 1,2. \quad (5)$$

Moreover, Eqs. (5) can be expressed in the compact form resulting in

$$\widehat{\sigma}_{ij} = C_{ijhk}^{EL}(\lambda(s))\,\widehat{\varepsilon}_{hk},$$

$$\widehat{D}_\alpha = -\beta^{EL}_{\alpha\alpha}(\lambda(s))\frac{\partial\widehat{\phi}}{\partial x_\alpha}, \qquad i,j,h,k,\alpha = 1,2. \tag{6}$$

It is worth-noting that the in-plane constitutive equations of an out-of-plane polarized piezoelectric continuum turn out to be uncoupled and, therefore, formally equivalent to the equations of a linear elastic dielectric material [98]. Thus, the components of the equivalent constitutive tensors pertaining to the shunting piezoelectric material result as

$$C^{EL}_{ijhk}(\lambda(s)) = C_{ijhk} + \frac{e_{ij3}\widetilde{e}_{3hk}}{\beta^{EL}_{33}(\lambda(s))} + \\ - \left(C_{ij33} + \frac{e_{ij3}\widetilde{e}_{333}}{\beta^{EL}_{33}(\lambda(s))}\right)\left(\frac{C_{33hk} + \frac{e_{333}\widetilde{e}_{3hk}}{\beta^{EL}_{33}(\lambda(s))}}{C_{3333} + \frac{e_{333}\widetilde{e}_{333}}{\beta^{EL}_{33}(\lambda(s))}}\right),$$

$$\beta^{EL}_{\alpha\alpha} = \beta_{\alpha\alpha} + \frac{e_{\alpha3\alpha}\widetilde{e}_{\alpha\alpha3}}{C_{\alpha3\alpha3}}, \qquad i,j,h,k,\alpha = 1,2, \tag{7}$$

with the components C^{EL}_{ijhk} explicitly depending on the tuning function $\lambda(s)$, except for the component C^{EL}_{1212} that is independent on $\lambda(s)$. Note that, as expected, the equivalent elastic tensor satisfies the major and minor symmetries.

Equivalent purely capacitive electrical circuit

In the particular case of remarkable technological interest, in which the equivalent electrical circuit is characterized by a purely capacitive equivalent admittance, it results that the auxiliary function $\beta^{EL}_{33}(s)$ becomes s-independent, i.e. $\beta^{EL}_{33} = \beta_{33} + \mathcal{C}\frac{L^{(P)}}{A^{(P)}} = \beta_{33}(1+\lambda)$, being $Y^{SU}_{33}(s) = s\mathcal{C}$ and where $\lambda = (\mathcal{C}L^{(P)})/(\beta_{33}A^{(P)})$, with $\lambda \in \mathbb{R}$, plays the role of a tuning parameter directly related to the capacitance $\mathcal{C}$. Also negative values of λ can be considered, exploiting equivalent negative capacitance circuits as in [99]. It follows that the equivalent elastic components C^{EL}_{ijhk} in (7) are, in turn, depend on the tuning parameter λ and are s-independent.

In particular, in Fig. 3 the dependence of the elastic components C^{EL}_{ijhk} of the shunting piezoelectric material on the tuning variable is investigated in the case of the Polyvinylidene fluoride (PVDF), whose piezoelectric material properties are listed in the following Section 3. More specifically, in Fig. 3(a) the dimensionless components $C^{EL}_{1111}/C^{PVDF}_{1111} = C^{EL}_{2222}/C^{PVDF}_{2222}$ (blue curves) and $C^{EL}_{1122}/C^{PVDF}_{1122}$ (red curves) are depicted versus λ. The curves exhibit vertical asymptotes in correspondence of the *resonance* value of the tuning parameter λ_R, expressed in the following form

$$\lambda_R = -\left(1 + \frac{e_{333}}{C_{3333}\beta_{33}}\right). \tag{8}$$

It is worth noting that the resonance phenomenon occurs for a negative λ value corresponding to a negative purely capacitive equivalent admittance $\mathcal{C}$. Further horizontal asymptotes are approached as $\lambda \to \pm\infty$, corresponding to the following asymptotic values

$$C^{EL\infty}_{ijhk} = \lim_{\lambda\to\pm\infty} C^{EL}_{ijhk}(\lambda) = C_{ijhk} - \frac{C_{ij33}C_{hk33}}{C_{3333}}, \qquad i,j,h,k = 1,2. \tag{9}$$

Finally, for $\lambda = 0$ the equivalent elastic components C^{EL0}_{ijhk}, see highlighted points in Fig. 3(a), turn to be those of a standard piezoelectric material coupled with an equivalent electrical circuit characterized by zero capacitance (or also an open circuit case), resulting in

$$C^{EL0}_{ijhk} = C^{EL}_{ijhk}(\lambda = 0) = C_{ijhk} + \frac{e_{ij3}e_{hk3}}{\beta_{33}} + \\ - \frac{\left(C_{ij33} + \frac{e_{ij3}e_{333}}{\beta_{33}}\right)\left(C_{hk33} + \frac{e_{hk3}e_{333}}{\beta_{33}}\right)}{C_{3333} + \frac{(e_{333})^2}{\beta_{33}}}, \quad i,j,h,k = 1,2. \tag{10}$$

Fig. 3(b) shows, in log–log plot, the absolute value of the relative difference between the component C^{EL}_{ijhk} and the corresponding one evaluated in $\lambda = 0$, i.e. $\Delta C^{EL}_{ijhk} = |C^{EL}_{ijhk} - C^{EL0}_{ijhk}|/C^{EL0}_{ijhk}$, as a function of the shifted tuning variable $\lambda^* = \lambda - \lambda_R$, investigated for $\lambda \geq \lambda_R$. In particular, the positive values of $C^{EL}_{ijhk} - C^{EL0}_{ijhk}$ are plotted in solid lines, while the negative ones in dashed lines. As expected, an asymptotic behaviour is found for $\lambda^* = 1$. Furthermore, a stiffer behaviour is exhibited as λ^* approaches zero, while a softer behaviour is shown for $\lambda^* \to \infty$. In this context, it is shown that by adjusting the equivalent impedance of the electrical circuit, it is possible to properly tuning the constitutive properties of the piezoelectric shunting element. It follows that the acoustic behaviour of the active metamaterial can be suitably tuned in turn.

2.2. Governing equations of tunable metamaterials

We aim to investigating the acoustic wave propagation in the tunable metamaterial. In this regard, let us consider the periodic three-phase microstructured metamaterial in Fig. 2, with a piezoelectric phase shunted by a generic dissipative electrical circuit, described as a first order continuum in the framework of the in-plane linear theory.

The in-plane dynamic balance equations, in the transformed Laplace space, of the tunable infinite metamaterial are expressed in the following form

$$\frac{\partial\widehat{\sigma}_{ij}}{\partial x_j} + \widehat{b}_i = \rho s^2\widehat{u}_i, \qquad i,j = 1,2, \tag{11}$$

being $\widehat{\sigma}_{ij}$ and $\widehat{u}_i$ the in-plane stress components and the in-plane displacement components, respectively, $\widehat{b}_i$ the transformed source term (or body force) and ρ the mass density and x_j the components of the in-plane position vector $\mathbf{x} = x_j\mathbf{e}_j$, with $j = 1,2$.

By exploiting the constitutive relations

$$\widehat{\sigma}_{ij} = C^{\diamond}_{ijkl}(s)\frac{\partial\widehat{u}_k}{\partial x_l}, \qquad i,j,k,l = 1,2, \tag{12}$$

where the components $C^{\diamond}_{ijkl}$ of the constitutive tensor for the shunting piezoelectric phase are in general s-dependent and coincide with C^{EL}_{ijkl} expressed in (7), while for the other elastic phases are s-independent.

Because of the periodicity of the metamaterial, it is worth noting that both constitutive tensors and the mass density satisfy the $\mathfrak{A}$ periodicity, i.e.

$$C^{\diamond}_{ijkl}\left(\mathbf{x}+\mathbf{v}_\beta, s\right) = C^{\diamond}_{ijkl}\left(\mathbf{x}, s\right), \\ \rho\left(\mathbf{x}+\mathbf{v}_\beta\right) = \rho\left(\mathbf{x}\right), \qquad i,j,k,l = 1,2, \qquad \beta = 1,2, \quad \forall\mathbf{x}\in\mathfrak{A}, \tag{13}$$

being $\mathbf{v}_\beta$ the periodicity vector.

By plugging (12) in (11), the governing equation of the in-plane free Bloch wave propagation, i.e. with $\widehat{b}_i = 0$, in the transformed Laplace space results

$$\frac{\partial}{\partial x_j}\left(C^{\diamond}_{ijkl}(s)\frac{\partial\widehat{u}_k}{\partial x_l}\right) - \rho s^2\widehat{u}_i = 0, \qquad i,j,k,l = 1,2. \tag{14}$$

By exploiting the medium periodicity, it is possible to consider only a single Periodic Cell $\mathfrak{A}$ undergoing the following Floquet–Bloch boundary conditions

$$\widehat{u}^+_i = \widehat{u}^-_i e^{\iota k_j v^{(\beta)}_j}, \\ \widehat{\sigma}^+_{ir} = -\widehat{\sigma}^-_{ir}(m^{(\beta)}_r)^- e^{\iota k_j v^{(\beta)}_j}, \tag{15}$$

where $v^{(\beta)}_j$ are the components of the periodicity vector $\mathbf{v}_\beta = v^{(\beta)}_j\mathbf{e}_j$, and $(m^{(\beta)}_r)^\pm$ are the components of the outward normal

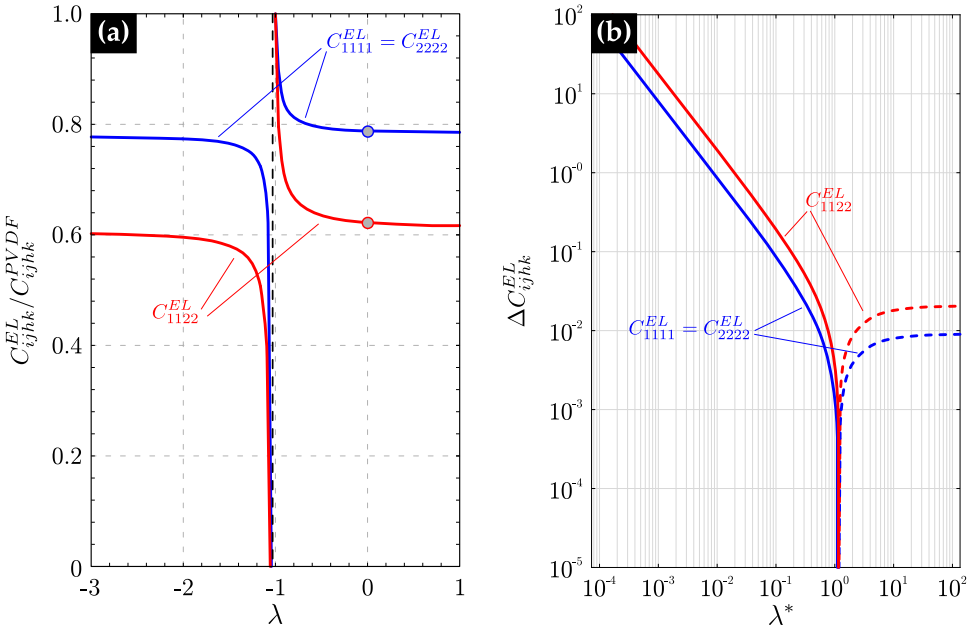

Fig. 3. (a) Dimensionless components of the equivalent constitutive tensors $C^{EL}_{ijhk}/C^{PVDF}_{ijhk}$ versus the tuning parameter λ. (b) $\Delta C^{EL}_{ijhk} = |C^{EL}_{ijhk} - C^{EL0}_{ijhk}|/C^{EL0}_{ijhk}$, versus the tuning variable λ^* in log–log plot. The blue curves refer to the components $C^{EL}_{1111} = C^{EL}_{2222}$, while the red curves refer to the components C^{EL}_{1122}. (For interpretation of the references to colour in this figure legend, the reader is referred to the web version of this article.)

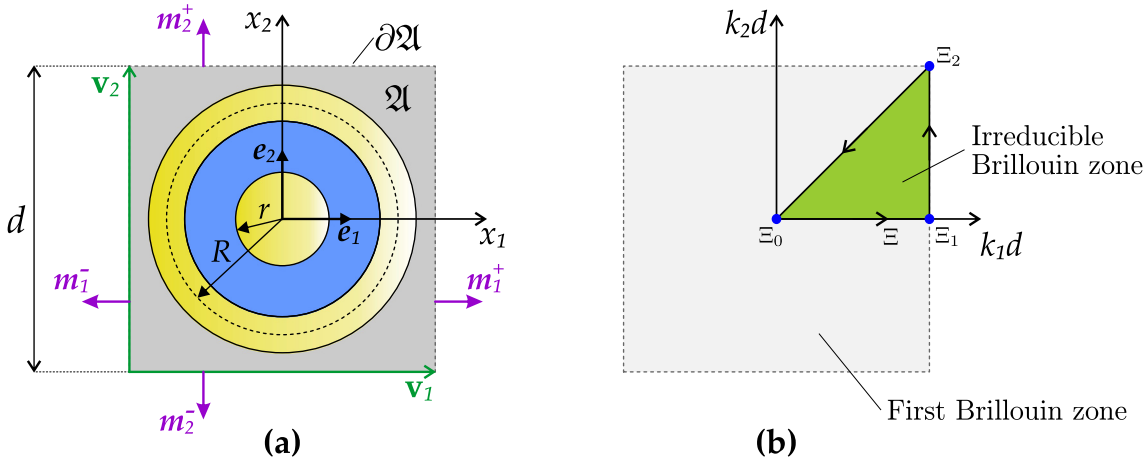

Fig. 4. (a) Periodic cell together with its periodicity vectors $\mathbf{v}_1$, $\mathbf{v}_2$; (b) First Brillouin zone and the irreducible Brillouin zone highlighted in green. (For interpretation of the references to colour in this figure legend, the reader is referred to the web version of this article.)

$\mathbf{m}^{\pm}_{\beta} = (m^{(\beta)}_j)^{\pm}\mathbf{e}_j$ to the boundary $\partial\mathfrak{A}$, $j, \beta = 1, 2$, see Fig. 4(a). In addition, the superscripts $^{\pm}$ refer to the positive part $\partial\mathfrak{A}^+$ (with outward normal $\mathbf{m}^+_\beta$) and to the corresponding negative parts $\partial\mathfrak{A}^-$ (with outward normal $\mathbf{m}^-_\beta$) of the Periodic Cell boundary. We recall that the following notation applies to the generic function $\widehat{g}$, i.e. $\widehat{g}^{\pm} \doteq \widehat{g}(\mathbf{x}^{\pm})$ where $\mathbf{x}^{\pm}$ identifies the generic point $P \in \partial\mathfrak{A}^{\pm}$, and $\mathbf{x}^+ = \mathbf{x}^- + \mathbf{v}_\beta$. Furthermore, k_j are the components of the wave vector $\mathbf{k}$. The dimensionless first Brillouin zone $\mathfrak{B} = [-\pi, \pi] \times [-\pi, \pi]$ is defined in the space of dimensionless wave vectors and is characterized by two orthogonal vectors $\pi\mathbf{n}_i$, parallel to $\mathbf{e}_i$, with $i = 1, 2$, coinciding with the periodicity vectors by virtue of the symmetry properties of the micro-structure, see Fig. 4(b). The solution of the differential eigen problem (14) with (15) leads in general to a complex-value frequency band structure, accordingly with the pioneering Floquet–Bloch theory [100–102].

Note that in the particular case of periodic material including a piezoelectric phase shunted by a non-dissipative electrical circuit or characterized by an equivalent purely capacitive electrical circuit, it can be proven that the complex frequency s turns to be purely imaginary, i.e. $s = \iota\omega$, being $\omega \in \mathbb{R}$ the angular frequency, and $\iota^2 = -1$. More specifically, in this case the differential eigen problem (14) takes the form

$$\frac{\partial}{\partial x_j}\left(C^{\diamond}_{ijkl}\frac{\partial \widehat{u}_k}{\partial x_l}\right) + \rho\omega^2\widehat{u}_i = 0, \qquad i, j, k, l = 1, 2. \tag{16}$$

together with the same Floquet–Bloch boundary conditions as in (15).

For the sake of completeness, the time domain governing equation of the in-plane free Bloch wave propagation in the periodic tunable metamaterial, shunted by a generic dissipative electrical circuit, can be determined by applying to (14) the inverse bilateral Laplace transform

$$\mathcal{L}^{-1}[\widehat{g}(\mathbf{x}, s)] = \frac{1}{2\pi\iota}\int_{r-\iota\infty}^{r+\iota\infty}\widehat{g}(\mathbf{x}, s)e^{st}ds, \qquad r \in \mathbb{R}. \tag{17}$$

It results that the following integro-differential equation is obtained

$$\frac{\partial}{\partial x_j}\left(\mathcal{L}^{-1}\left[\frac{C^{\diamond}_{ijkl}(s)}{s}\right] * \frac{\partial^2 u_k}{\partial x_l\,\partial t}\right) = \rho\frac{\partial^2 u_i}{\partial t^2} \qquad i,j,k,l = 1,2. \tag{18}$$

where $*$ is the convolution product, and the well-known property $\mathcal{L}(\partial^n g(\mathbf{x},t)/\partial t^n) = s^n \widehat{g}(\mathbf{x},s)$ is exploited. Note that such equation is formally analogous to the field equation of a periodic viscoelastic continuum, where the relaxation function $C^{\diamond}_{ijkl}(s)/s$ explicitly depends on the equivalent admittance of a generic electrical circuit.

In the particular case of purely capacitive equivalent admittance, where the constitutive equivalent components $C^{\diamond}_{ijkl}$ are s-independent, by applying to (16) the inverse Fourier transform

$$\mathcal{F}^{-1}\left[\widehat{g}(\mathbf{x},\omega)\right] = \frac{1}{2\pi}\int_{-\infty}^{+\infty} \widehat{g}(\mathbf{x},\omega)e^{\imath\omega t}d\omega, \tag{19}$$

the field equation in the time domain takes the following form

$$\frac{\partial}{\partial x_j}\left(C^{\diamond}_{ijkl}\frac{\partial u_k}{\partial x_l}\right) = \rho\frac{\partial^2 u_i}{\partial t^2}, \qquad i,j,k,l = 1,2, \tag{20}$$

that is formally analogous to the field equation of a periodic elastic first order continuum.

3. Numerical experiments

This Section is first devoted to characterize the frequency band structure of the proposed tunable acoustic metamaterial for different geometric design parameters (Section 3.1). Furthermore, a numerical experiment is proposed to test the effectiveness of the periodic tunable metamaterial as acoustic filter (Section 3.2).

3.1. Tuning of pass and stop bands

Here we investigate the in-plane dynamic response of the tunable acoustic metamaterial reported in Fig. 2(b), where also the relevant dimensions are depicted. The radius of the resonator and the mean radius of the external ring are denoted by r and R, respectively, while the edge of the square periodic cell is d. We assume that the soft matrix is made of Epotex 301, a passive polymer materials, with elastic properties $E = 3.6$ GPa and $\nu = 0.35$, and mass density $\rho = 1150$ kg/m^3, see [103]. Both the outer ring and the circular resonator are made of steel with $E = 210$ GPa, $\nu = 0.3$ and mass density $\rho = 7500$ kg/m^3. Focusing on the state of plane stress of such two materials, the non-vanishing components of the elasticity tensor are determined as $C^{\diamond}_{1111} = C^{\diamond}_{2222} = E/(1-\nu^2)$, $C^{\diamond}_{1122} = \nu E/(1-\nu^2)$, $C^{\diamond}_{1212} = E/2(1+\nu)$. Finally, the shunted piezoelectric element is designed by connecting a Polyvinylidene fluoride (PVDF, mass density $\rho = 1780$ kg/m^3) ring to an electrical circuit characterized by purely capacitive equivalent admittance, as schematically shown in Fig. 2(b). In this way, by modifying the tuning parameter λ (introduced in Section 2.1), directly related to the equivalent impedance of the electrical circuit, it is possible to properly adjust the equivalent constitutive properties of the shunted piezoelectric element. The electromechanical properties of PVDF, polarized along the $\mathbf{e}_3$ direction, are taken from [104] and are listed below. The non vanishing components of the elasticity tensor are $C_{1111} = C_{2222} = 4.84\cdot 10^{09}$ Pa, $C_{3333} = 4.63\cdot 10^{9}$ Pa, $C_{1122} = 2.72\cdot 10^{9}$ Pa, $C_{1133} = C_{2233} = 2.22\cdot 10^{9}$ Pa, $C_{1212} = 1.06\cdot 10^{9}$ Pa, $C_{1313} = C_{2323} = 5.26\cdot 10^{7}$ Pa. The non vanishing components of the stress–charge coupling tensor are $e_{113} = e_{223} = -1.999\cdot 10^{-3}$ C/m^2, $e_{311} = e_{322} = 4.344\cdot 10^{-3}$ C/m^2, $e_{333} = -1.099\cdot 10^{-1}$ C/m^2. The set of components is complemented by the non vanishing components of the dielectric permittivity tensor, i.e. $\beta_{11} = \beta_{22} = 6.641\cdot 10^{-11}$ C/Vm, and $\beta_{33} = 7.083\cdot 10^{-11}$ C/Vm. The corresponding in-plane constitutive components of the shunted piezoelectric material, characterized by $\widehat{I}_3 = 0$, $\widehat{\sigma}_{i3} = 0$ with $i = 1,2,3$, are obtained by exploiting the Eqs. (7) in Section 2.1, where $C_{ijhk} = C^{EL}_{ijhk}$, and $\beta_{ij} = \beta^{EL}_{ij}$, with $i,j,h,k = 1,2$, specialized to the case of tuning function $\lambda(s) = (\mathcal{C}L^{(P)})/(\beta_{33}A^{(P)})$.

We aim to study the influence of a set of geometric parameters, characterizing the periodic cell, on the Floquet–Bloch spectrum of the metamaterial as the tuning parameter λ changes. In this regard, different periodic cells are taken into account, which differs for the ratios r/R and R/d, taking the ratios $h/d = 0.075$, $w/d = 1$, with the edge of the periodic cell $d = 1$ cm. For the sake of clarity a simple schematic of the geometry together with the relevant dimensions is depicted in Fig. 4(a). Attention is focused on the acoustic band structure of the metamaterial in the first irreducible Brillouin zone (highlighted in green in Fig. 4(b)) defined within the closed polygonal curve Γ, joining the vertices Ξ_0, Ξ_1 and Ξ_2 placed on the curvilinear abscissa Ξ in the dimensionless plane $(k_1 d, k_2 d)$. To this aim the governing equation of the in-plane free Bloch wave propagation (16) together with the associated Floquet–Bloch boundary conditions (15) are solved in the periodic cell exploiting the finite element method. Triangular elements with quadratic Lagrangian interpolation functions have been adopted. Note that due to the centro-symmetry of the periodic cell, the curve Γ delimits the first irreducible Brillouin zone.

First, three cases are considered characterized by $r/R = 0.5$ and variable R/d. In Figs. 5–7, the ratio R/d takes values 0.3, 0.35 and 0.4, respectively. In all cases the comparison of the Floquet–Bloch spectrum obtained for $\lambda = 0$, in figures (a), and $\lambda \approx \lambda_R \simeq -1.0368$, in figures (b), is performed. The curves report the values of the dimensionless angular frequency $\omega d\sqrt{\rho^{PVDF}/C^{PVDF}_{3333}}$, against the curvilinear abscissa Ξ. The first 20 branches of the spectrum are taken into account. More specifically, the case with the smallest resonator ($R/d = 0.3$) is shown in Fig. 5. By comparing the results obtained for $\lambda = 0$, Fig. 5(a), i.e. the case of standard (non shunted) piezoelectric ring, with those for $\lambda \approx \lambda_R$ i.e. *resonant* value, Fig. 5(b), it emerges that the total low-frequency band gap, between the 1st and the 2nd optical branches, becomes noticeably wider. Moreover, the two acoustic branches and the 1st optical branch remain almost unchanged as λ varies, while in the considered frequency range a higher spectral density is detected for the remaining optical branches.

In Fig. 6 the case with $R/d = 0.35$ is taken into account. In this case for $\lambda = 0$, Fig. 6(a), three total band gaps are found. Indeed, besides the wider low frequency band gap, between the first and the second optical branches, two more narrow band gaps appear at higher frequencies in the considered range (between the 6th and the 7th optical branches and between the 11th and the 12th optical branches, respectively). Passing to $\lambda \approx \lambda_R$, in Fig. 6(b), it is noticed that the low frequency band gap opens, the two further total band gaps disappear, while a new total band gap forms between the 8th and the 9th optical branches.

Finally, in Fig. 7 the ratio $R/d = 0.4$ is considered. By comparing the Floquet–Bloch spectra for $\lambda = 0$ and $\lambda \approx \lambda_R$, it stands to reason that in the first case, Fig. 7(a), a very dense spectrum is found, with acoustic optical branches intersecting each other over and over, without total band gaps. On the other hand, in the second case, Fig. 7(b), a wide low frequency band gap is detected, together with three further total band gaps opening between optical branches 6th–7th, 12th–13th and 13th–14th, respectively.

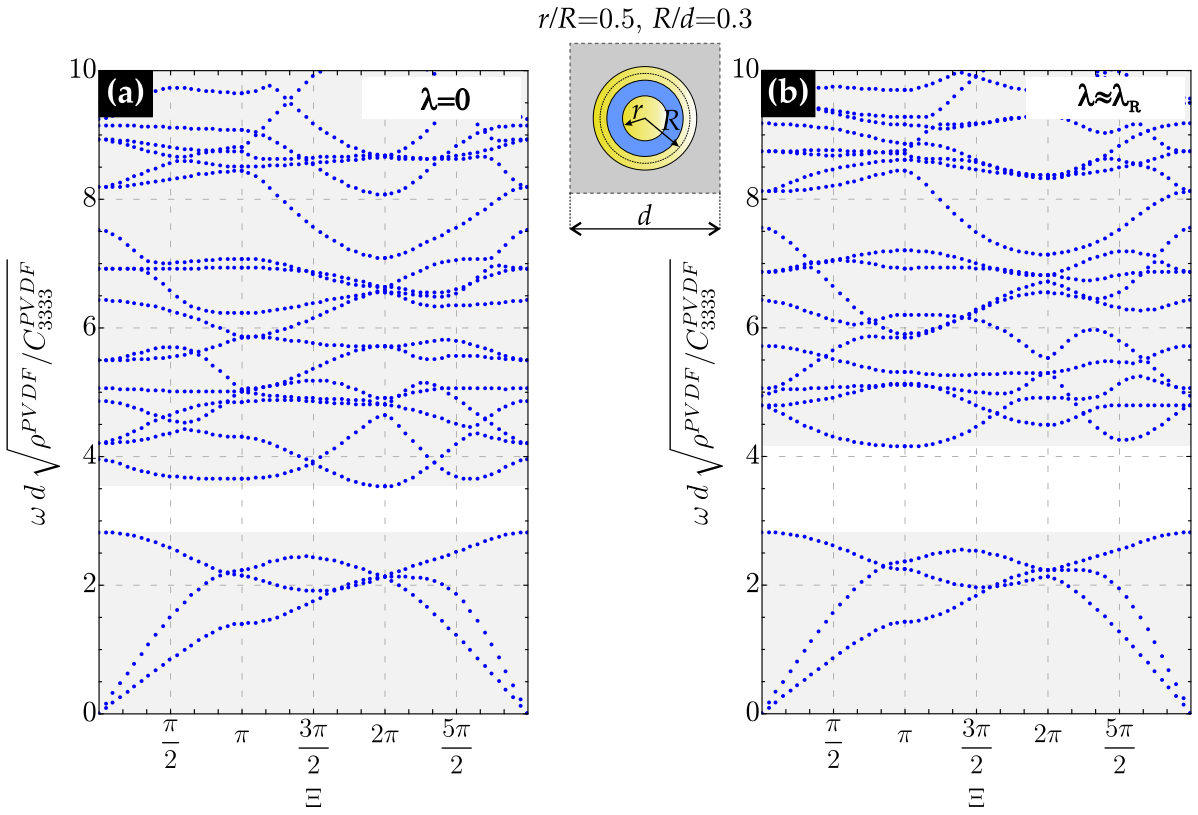

Fig. 5. Floquet–Bloch spectrum for the metamaterial with $r/R = 0.5$ and $R/d = 0.3$ in terms of the dimensionless frequency $\omega d\sqrt{\rho^{PVDF}/C_{3333}^{PVDF}}$ versus the curvilinear abscissa Ξ. (a) Tuning parameter $\lambda = 0$; (b) tuning parameter $\lambda \approx \lambda_R$.

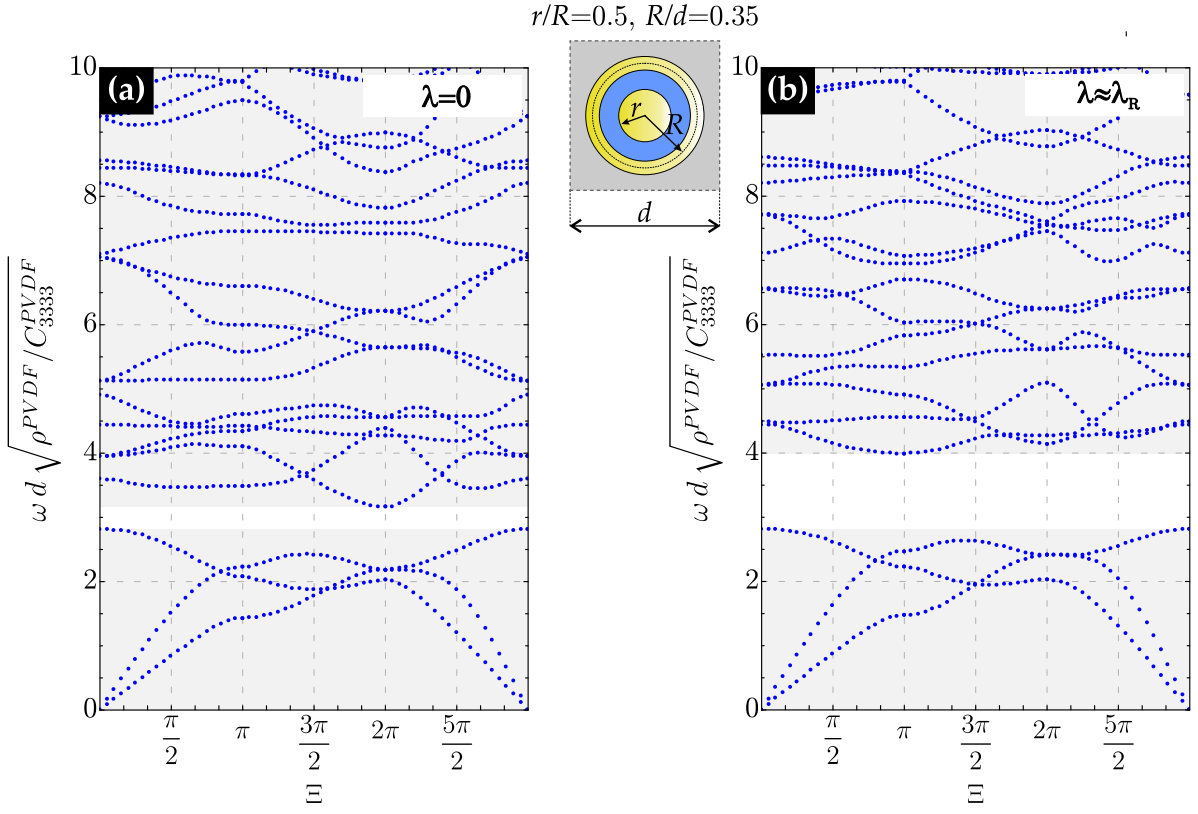

Fig. 6. Floquet–Bloch spectrum for the metamaterial with $r/R = 0.5$ and $R/d = 0.35$ in terms of the dimensionless frequency $\omega d\sqrt{\rho^{PVDF}/C_{3333}^{PVDF}}$ versus the curvilinear abscissa Ξ. (a) Tuning parameter $\lambda = 0$; (b) tuning parameter $\lambda \approx \lambda_R$.

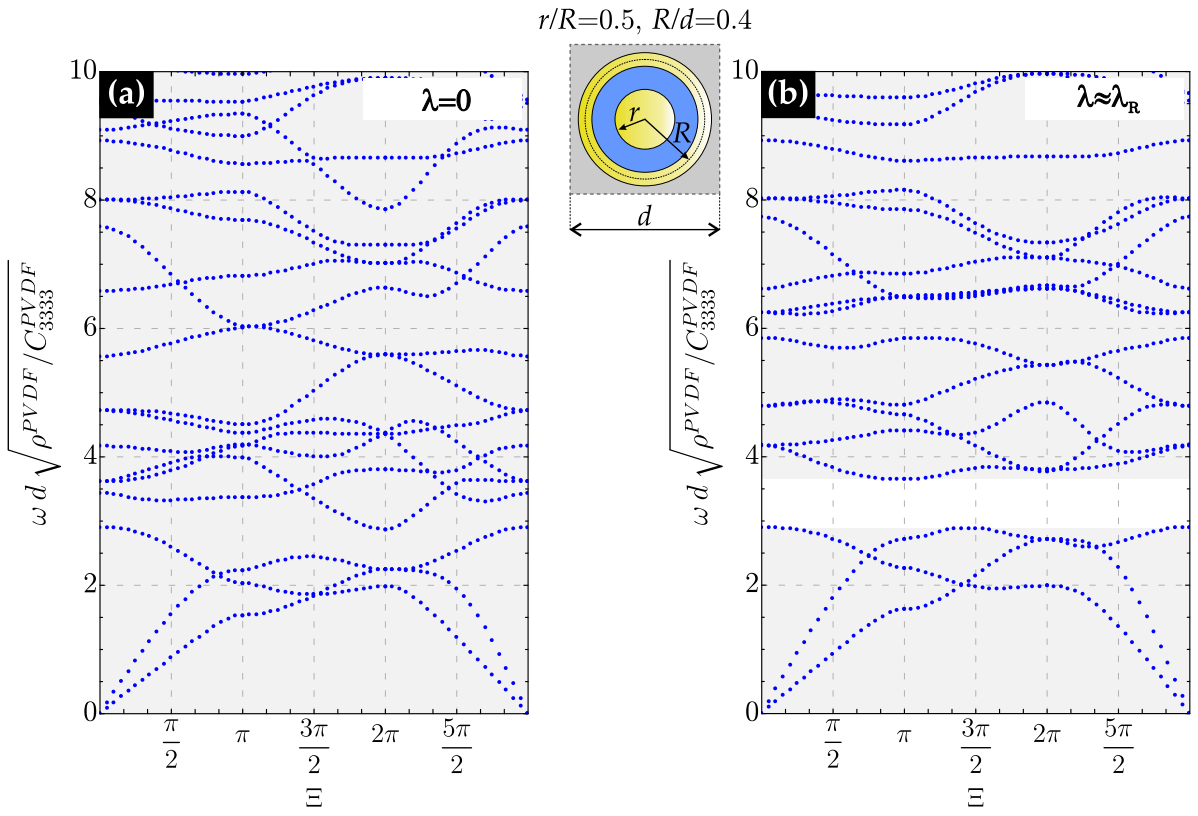

Fig. 7. Floquet–Bloch spectrum for the metamaterial with $r/R = 0.5$ and $R/d = 0.4$ in terms of the dimensionless frequency $\omega d\sqrt{\rho^{PVDF}/C^{PVDF}_{3333}}$ versus the curvilinear abscissa Ξ. (a) Tuning parameter $\lambda = 0$; (b) tuning parameter $\lambda \approx \lambda_R$.

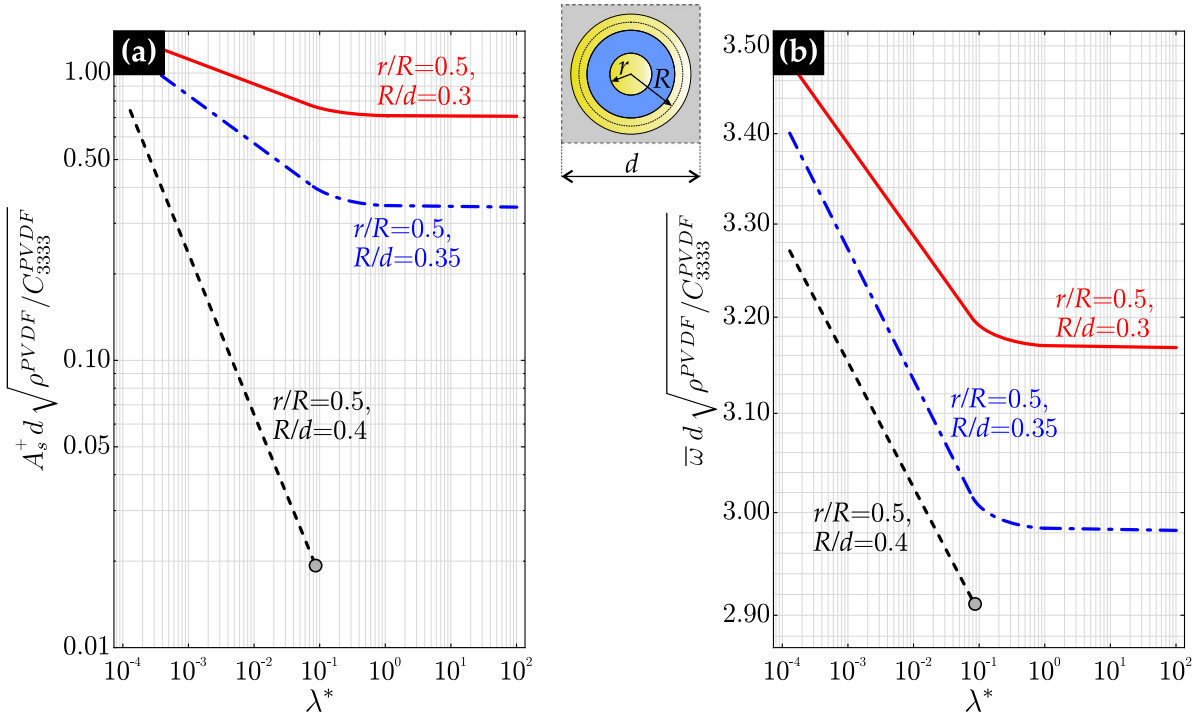

Fig. 8. Behaviour of the metamaterial with $r/R = 0.5$ and $R/d = 0.3$ (blue curves); $R/d = 0.35$ (red curves) and $R/d = 0.4$ (black curves). (a) Dimensionless band gap amplitude $A_s^+ d\sqrt{\rho^{PVDF}/C^{PVDF}_{3333}}$ versus the tuning parameter $\lambda^* = \lambda - \lambda_R$; (b) Central frequency $\overline{\omega} d\sqrt{\rho^{PVDF}/C^{PVDF}_{3333}}$ versus the tuning parameter $\lambda^* = \lambda - \lambda_R$. (For interpretation of the references to colour in this figure legend, the reader is referred to the web version of this article.)

To sum up, it can be observed that the geometry of the metamaterial, i.e. the relative size of its elastic and shunting piezoelectric elements, has a significant impact on the operation of the device with or without triggering the shunting effect, that is for $\lambda \approx \lambda_R$ and $\lambda = 0$.

A further investigation has been performed by comparing the results obtained for the three geometries considered so far, in terms of both dimensionless band gap amplitude $A_s^+ d\sqrt{\rho^{PVDF}/C_{3333}^{PVDF}}$ and central frequency $\overline{\omega} d\sqrt{\rho^{PVDF}/C_{3333}^{PVDF}}$ versus the tuning parameter $\lambda^* = \lambda - \lambda_R$. Attention is focused on the first band gap forming between the 1st and the 2nd optical branches of the Floquet–Bloch spectrum. In Fig. 8 the blue curve refers to the ratio $R/d = 0.3$, the red curve to $R/d = 0.35$, and the black curve refers to $R/d = 0.4$. It can be noted irrespective of the considered geometry, the band gap amplitude, Fig. 8(a), and the central frequency, Fig. 8(b), increase as λ^* decreases, i.e. when λ tends to λ_R. The maximum amplitude is guaranteed by the metamaterial with the smallest radii r and R. Moreover, a peculiar trend is observed for $R/d = 0.4$, since in this case it is possible to open a band gap and controlling its amplitude and central frequency by intervening on the tuning parameter λ, starting from a dense spectrum for $\lambda = 0$. The analysis of additional geometries characterizing the metamaterial reveals that the use of ratios $r/R = 0.7$ and $R/d = 0.4$ ensures a wide range of behaviours as λ changes. In Fig. 9 the Floquet–Bloch spectrum referred to this geometry is shown for different values of λ. Specifically, Fig. 9(a) shows the curve related to $\lambda = 0$. Note that in this case, where the shunting effects are not triggered, a wide total band gap is detected between the 1st and the 2nd optical branches. As λ decreases further band gaps opens, as in Fig. 9(b) corresponding to $\lambda = -1.0100$, in which a new total band gap forms between the 15th and the 16th optical branches. Moving towards a lower value of $\lambda = -1.0334$, Fig. 9(c), besides the first band gap, three additional total band gaps open between the 2nd–3rd, 5th–6th, 12th–13th optical branches, respectively. Finally, when λ_R is approached as in Fig. 9(d) with $\lambda = -1.0368$, the first band gap remains almost unchanged, while the two additional total band gaps at low frequencies, between the 2nd–3rd, 4th–5th optical branches, becomes wider. In the considered frequency range the spectrum tends to become less dense as λ decreases. Moreover, in Fig. 10 the wave forms of the Floquet–Bloch spectrum for the metamaterial with $r/R = 0.7$ and $R/d = 0.4$ for $\lambda \approx \lambda_R$, related to relevant points highlighted in Fig. 9(d), are reported. In particular, the deformed shape together with the contour plot related to the dimensionless quantity $\|\mathrm{Re}(\widehat{\boldsymbol{u}})\|_2/d$ are shown. Also in this case we investigate the behaviour of the metamaterial in terms of both dimensionless band gap amplitude $A_s^+ d\sqrt{\rho^{PVDF}/C_{3333}^{PVDF}}$, Fig. 11(a), and central frequency $\overline{\omega} d\sqrt{\rho^{PVDF}/C_{3333}^{PVDF}}$, Fig. 11(b), versus the tuning parameter $\lambda^* = \lambda - \lambda_R$.

The first two lower band gaps, forming between the 1st–2nd and 2nd–3rd optical branches, are analysed. In particular, the blue curves refer to the lowest frequency total band gap, while the red curves are referred to the other band gap. The band gap amplitude, associated to the blue curve in Fig. 11(a), tends to increase as λ^* decreases. As expected, analogous behaviour is detected for the corresponding central frequency in Fig. 11(b). On the other hand, concerning the red curves, an interesting behaviour is observed related to the formation of a new total band gap from a dense spectrum

3.2. Filtering performances of the tunable metamaterial

In order to assess the filtering properties of the proposed tunable metamaterial we here present a numerical experiment developed in Abaqus. We consider the specimen depicted in Fig. 12, made up of a thin rectangular strip of homogeneous material in which a central stripe has been replaced by a cluster of ten by five periodic cells of the designed metamaterial. The specimen has dimensions $L_1 = 250$ mm, $L_2 = 100$ mm and uniform thickness w, while the geometry of the periodic cell is the same adopted in Fig. 9, i.e. characterized by $r/R = 0.7$ and $R/d = 0.4$, with the edge $d = 10$ mm. More specifically, the homogeneous material is made of epoxy resin (EPO-TEK® 301) such as the soft matrix of the metamaterial (see Section 3).

The left and right sides of the specimen are fully clamped, while the bottom and top sides are subject to free boundary conditions. As excitation source, an in-plane mono-frequency time-harmonic displacement excitation $u_2 = \mathcal{U}\sin(\Omega t)$ has been imposed to the left side, being $\mathcal{U} = 0.01$ mm the excitation amplitude and Ω its angular frequency. The geometry of the sample has been designed in SolidWorks and then imported in Abaqus. The specimen has been discretized using S4R elements. Mesh size and time step were carefully chosen accordingly to the Courant–Friedrichs–Lewy (CFL) condition and Blake's criteria [105,106]. More specifically, the higher is the frequency, the smaller has to be the mesh size and the time step. In particular, we performed a mesh-refinement study to estimate the optimal mesh-size so that the results to be mesh-independent. The numerical simulation of the undamped dynamic response has been achieved by means of an dynamic/explicit time-stepping scheme.

Depending on the excitation frequency, qualitatively different behaviours are observed. More specifically, in the case shown in Fig. 13(a), i.e. when the dimensionless excitation frequency Ω/Ω_r, being $\Omega_r = \left(d\sqrt{\rho^{PVDF}/C_{3333}^{PVDF}}\right)^{-1}$, falls within the first low-frequency pass band highlighted in Fig. 9(d) in black/dashed line, with the tuning parameter $\lambda \approx \lambda_R$, a marked propagation of acoustic waves through the metamaterial core is found.

Looking at the contour plots of the dimensionless displacement magnitudes u/u_{max}, defined as the ratio between $u = \|u_i \mathbf{e}_i\|_2$, with $i = 1, 2$, and the respective maximum value u_{max}, that are referred to different instants of time t/t_r, with $t_r = d\sqrt{\rho^{PVDF}/C_{3333}^{PVDF}}$, it emerges, indeed, that the wave-front propagates starting from the left side and at the dimensionless time about $t/t_r = 0.016$ it reaches the microstructured core. After various diffraction, reflection and refraction phenomena, the advancing wave-front propagates through the metamaterial at dimensionless times greater than $t/t_r = 0.024$ without noticeable attenuation in the excitation amplitude.

The wave propagation is also confirmed by the time histories of the dimensionless displacement magnitudes u/d, black curves in Fig. 14, measured at equispaced control points. All the points are characterized by displacement magnitudes quantitatively comparable with each other, this means that the metamaterial does not give rise to wave trapping effect, so that it does not act as acoustic filter. On the other hand, in the case depicted in Fig. 13(b), i.e. when the excitation frequency falls within the first low-frequency stop band, highlighted in Fig. 9(d) in green/dash–dot line, with the tuning parameter $\lambda \approx \lambda_R$, the metamaterial core is definitely able to act as a filter. In this case, by observing the contour plots of the dimensionless displacement magnitudes u/u_{max}, it is evident that, as in the previous case, the wave-front propagates starting from the left side and at about the same dimensionless time $t/t_r = 0.016$ it reaches the microstructured core, giving rise to diffraction, reflection and refraction phenomena. Conversely, the propagating acoustic wave is trapped in the metamaterial core, that works as a metafilter, as shown at dimensionless times greater than $t/t_r = 0.024$. Also in this case, this behaviour is confirmed by the

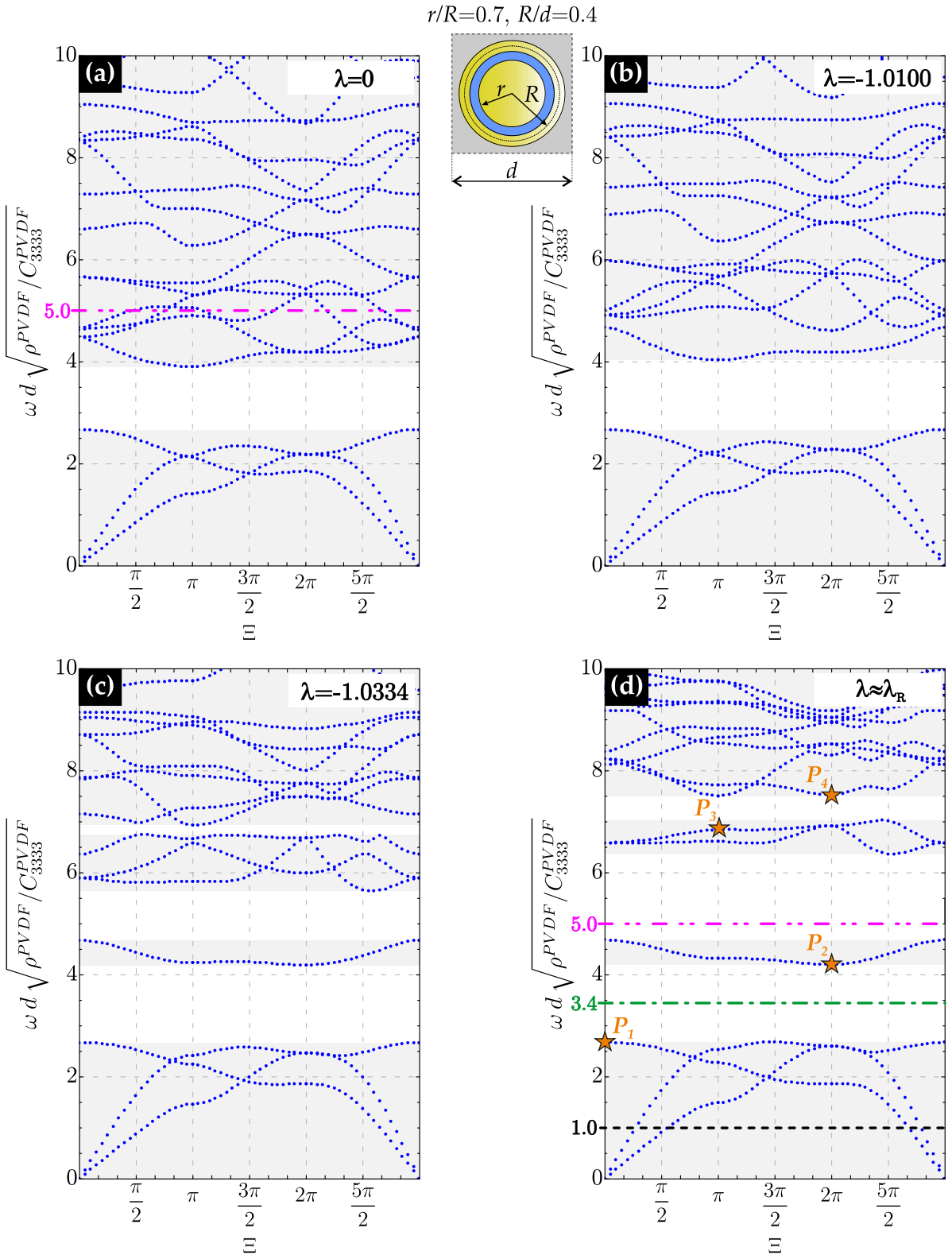

Fig. 9. Floquet–Bloch spectrum for the metamaterial with $r/R = 0.7$ and $R/d = 0.4$ in terms of the dimensionless frequency $\omega d\sqrt{\rho^{PVDF}/C_{3333}^{PVDF}}$ versus the curvilinear abscissa Ξ. (a) Tuning parameter $\lambda = 0$; (b) tuning parameter $\lambda = -1.0100$; (c) tuning parameter $\lambda = -1.0334$; (d) tuning parameter $\lambda \approx \lambda_R$. In the subfigure (d), are also reported the dimensionless excitation frequencies ($\Omega/\Omega_r = 1$ and 3.4) exploited in the numerical experiments reported in Section 3.2.

time histories of the dimensionless displacement magnitudes u/d, green curves in Fig. 14, measured at the same equispaced control points. By comparing the displacement magnitudes pertaining to points A and D, it is noted that the latter values are almost negligible with respect to the former ones. Moreover, as expected the displacement magnitudes in C is noticeably lower than that in B.

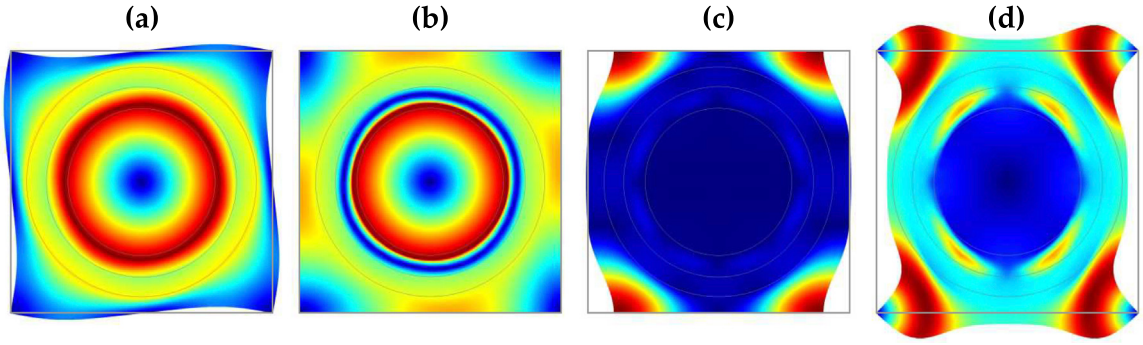

Fig. 10. Wave forms related to some relevant points of the Floquet–Bloch spectrum for the metamaterial with $r/R = 0.7$ and $R/d = 0.4$ for $\lambda \approx \lambda_R$ as reported in Fig. 9(d). (a) Point P_1 in the 1st optical branch; (b) Point P_2 in the 2nd optical branch; (c) Point P_3 in the 4th optical branch; (d) Point P_4 in the 5th optical branch.

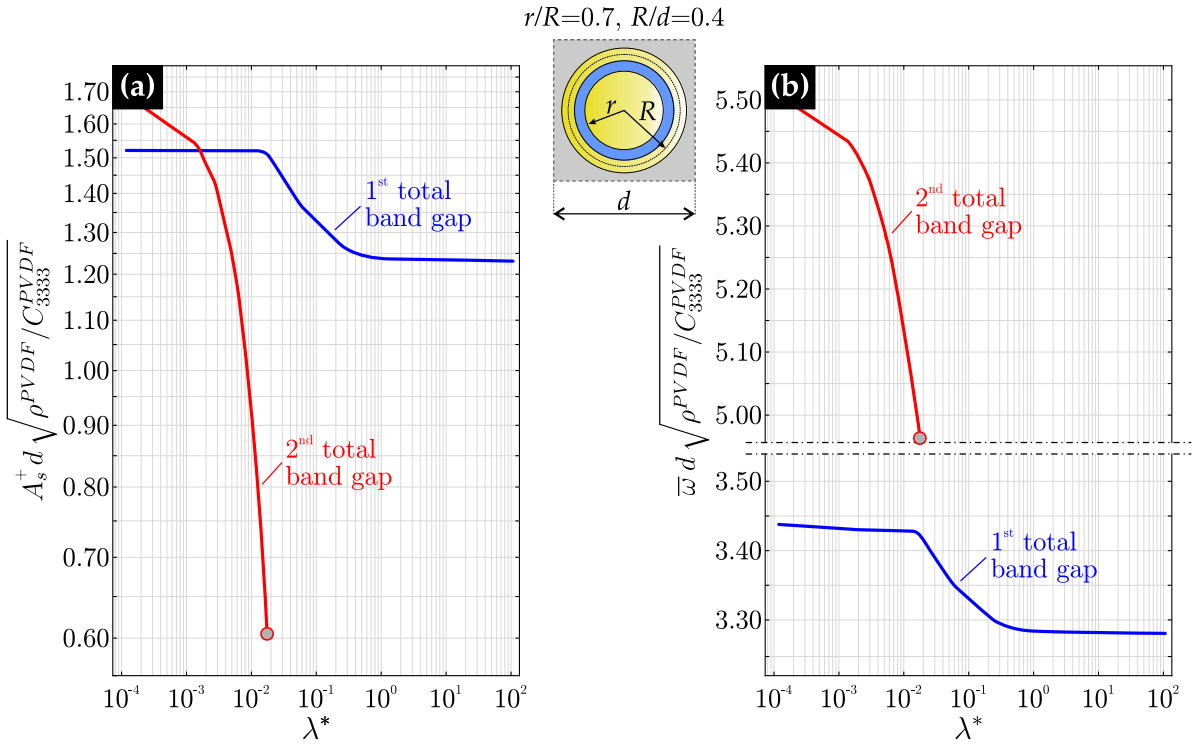

Fig. 11. First (blue curve) and second (red curve) total band gaps for the metamaterial with $r/R = 0.7$ and $R/d = 0.4$. (a) Dimensionless band gap amplitude $A_s^+ d\sqrt{\rho^{PVDF}/C_{3333}^{PVDF}}$ versus the tuning parameter $\lambda^* = \lambda - \lambda_R$; (b) Central frequency $\overline{\omega} d\sqrt{\rho^{PVDF}/C_{3333}^{PVDF}}$ versus the tuning parameter $\lambda^* = \lambda - \lambda_R$. (For interpretation of the references to colour in this figure legend, the reader is referred to the web version of this article.)

A further investigation aimed at showing the filtering performances of the tunable metamaterial as the tuning parameter changes is also performed. In particular, in the case shown in Fig. 15(a), i.e. for tuning parameter $\lambda = 0$ and dimensionless excitation frequency $\Omega/\Omega_r = 5$, falling within the first low-frequency pass band highlighted in Fig. 9(a) in magenta/dash-double dot line, a marked propagation of acoustic waves through the metamaterial core is found. Considering the contour plots of the dimensionless displacement magnitudes u/u_{max}, referred to different instants of time t/t_r, it appears that the wave-front propagates from the left side and at the dimensionless time about $t/t_r = 0.016$ it reaches the microstructured core. After various diffraction, reflection and refraction phenomena, the advancing wave-front propagates through the metamaterial at dimensionless times greater than $t/t_r = 0.026$ without noticeable attenuation in the excitation amplitude. Also in this case, the wave propagation is confirmed by the time histories of the dimensionless displacement magnitudes u/d, grey curves in Fig. 16, measured at equispaced control points. All the points are characterized by displacement magnitudes quantitatively comparable with each other, i.e. the metamaterial does not act as acoustic filter.

Conversely, in the case depicted in Fig. 15(b), i.e. for tuning parameter $\lambda \approx \lambda_R$ and dimensionless excitation frequency $\Omega/\Omega_r = 5$, falling within the second frequency stop band, highlighted in Fig. 9(d) in magenta/dash-double dot line, the metamaterial core is certainly able to act as a filter. Also in this case, by observing the contour plots of the dimensionless displacement magnitudes u/u_{max}, it is evident that the wave-front propagates from the left side and at about the same dimensionless time $t/t_r = 0.016$ it reaches the microstructured core, giving rise to diffraction, reflection and refraction phenomena. On the other hand, the propagating acoustic wave is trapped in the metamaterial core, working as a metafilter, as shown at dimensionless times greater than $t/t_r = 0.026$. This behaviour is again confirmed by the time histories of the dimensionless displacement magnitudes u/d,

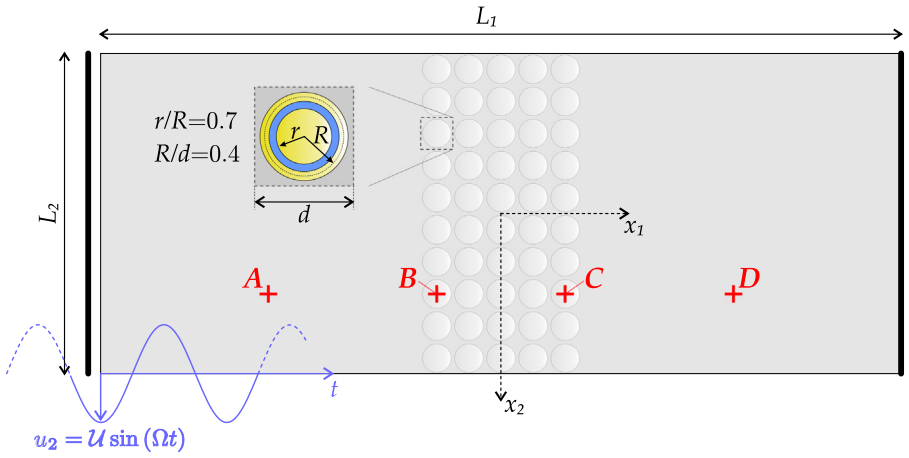

Fig. 12. Thin rectangular strip of homogeneous material with a central core made by a portion of the metamaterial, undergoing a mono-frequency time-harmonic in-plane displacement excitation.

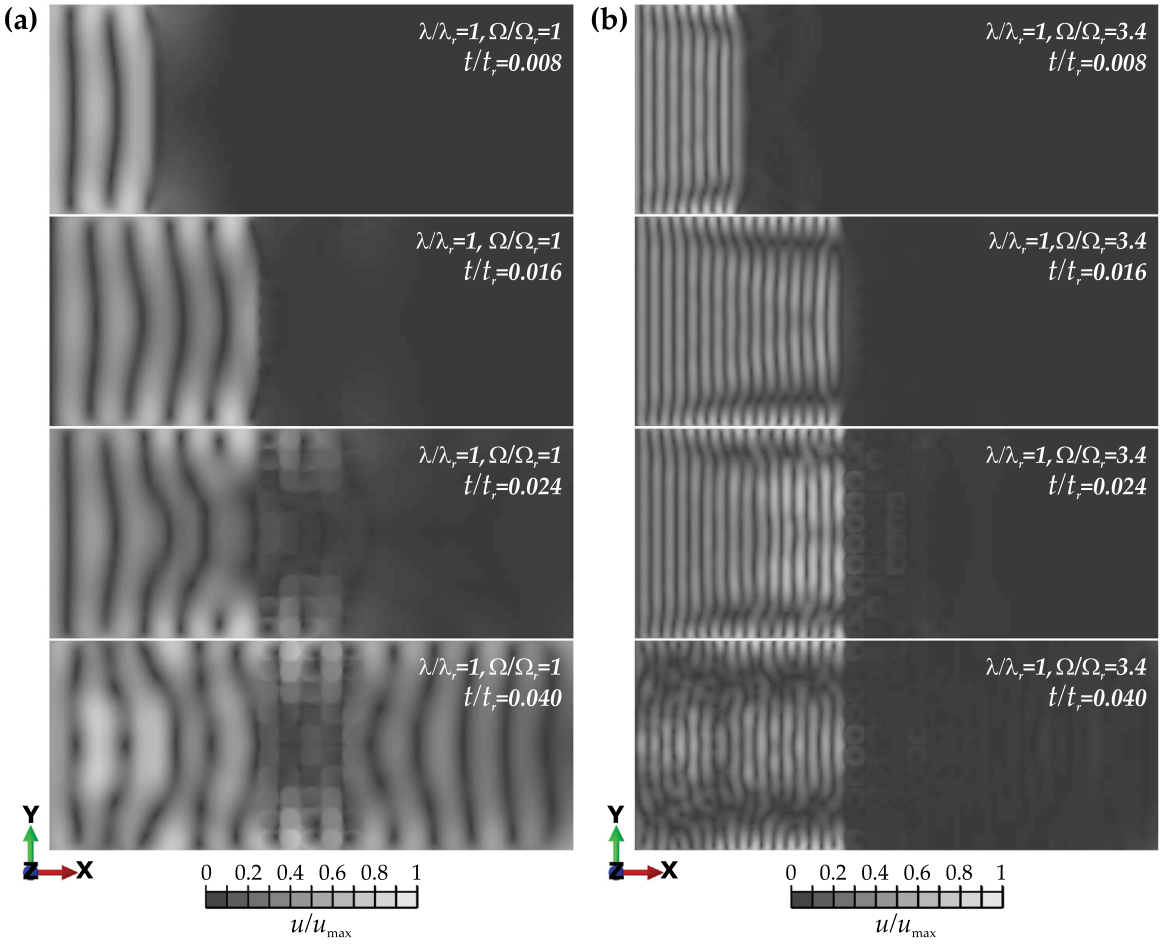

Fig. 13. Contour plots of the dimensionless displacement magnitudes u/u_{max} at different dimensionless time instants t/t_r. (a) dimensionless excitation frequency $\Omega/\Omega_r = 1$; (b) dimensionless excitation frequency $\Omega/\Omega_r = 3.4$.

blue curves in Fig. 16, measured at the same equispaced control points. By comparing the displacement magnitudes pertaining to points *A* and *D*, it is noted that the latter values are almost negligible with respect to the former ones. Moreover, as expected the displacement magnitudes in *C* is noticeably lower than that in *B*. A couple of videos showing the filtering performances of the tunable metamaterial are available as supplementary material.

4. Final remarks

A class of tunable acoustic metamaterials with periodic piezoelectric microstructure, shunted by an electrical circuit and characterized by adjustable frequency band structure is here proposed. The main goal is the design of high-performance acoustic

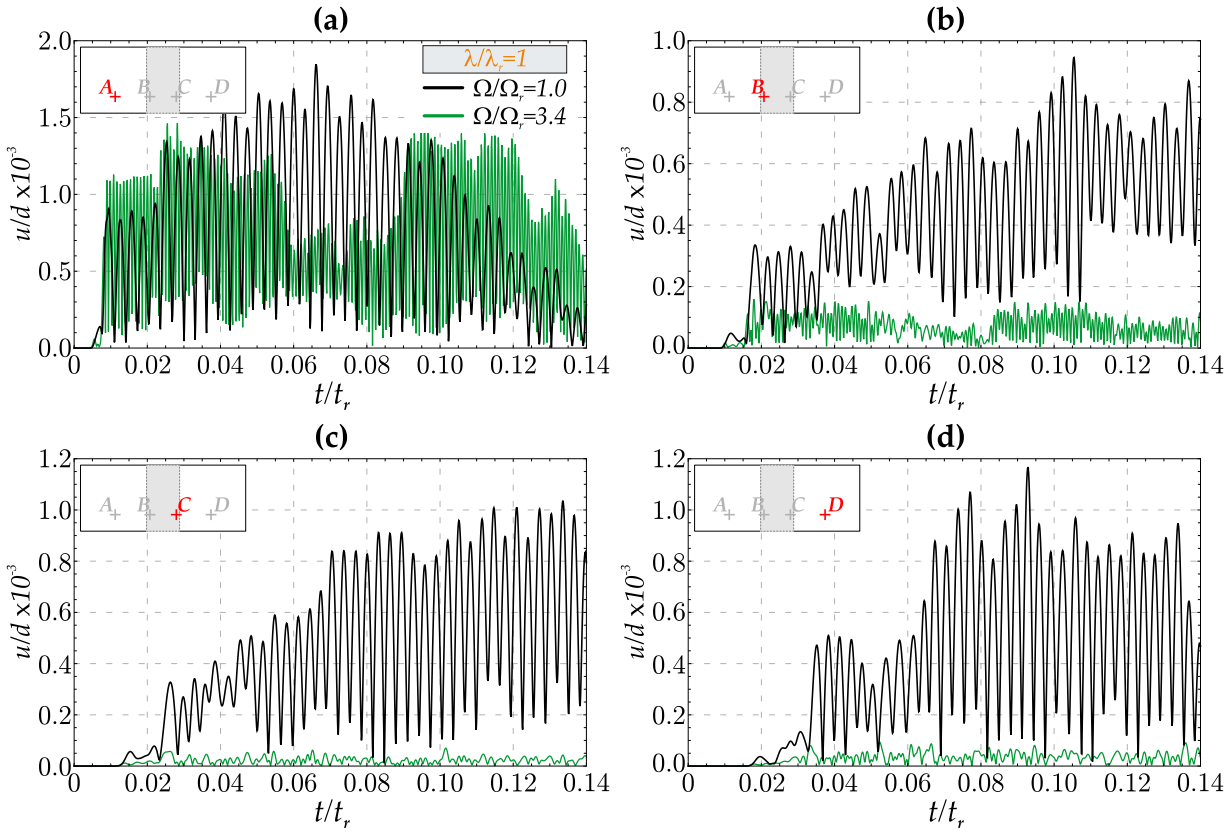

Fig. 14. Time histories of the dimensionless displacement magnitudes u/d versus the dimensionless time t/t_r for two characteristic values of the dimensionless excitation frequency Ω/Ω_r in four control points: (a) point A; (b) point B; (c) point C; (d) point D. (For interpretation of the references to colour in this figure legend, the reader is referred to the web version of this article.)

filters for the adaptive passive control of wave propagation in periodic materials. Attention is paid to three-phase microstructured materials made of a phononic crystal coupled to local resonators. In particular, the periodic phononic crystal is characterized by an in-plane regular repetition of rigid and heavy external rings embedded within a soft and light matrix. On the other hand, the local resonators are made of rigid and heavy internal disks connected to the external rings through inner rings made of a piezoelectric material shunted by an electrical circuit. In the framework of a micromechanical approach, the dispersive waves propagation within the periodic medium has been analysed, by exploiting a generalization of the Floquet–Bloch theory, in order to determine the frequency band structure of such materials. The governing equations of the in-plane Bloch-wave propagation have been introduced, complemented by their associated Floquet–Bloch boundary conditions. The constitutive equations of the orthotropic shunted piezoelectric material have been derived in the Laplace transformed space. In the case the piezoelectric phase is shunted by a generic dissipative electrical circuit, the components of the constitutive tensors are in general dependent on the complex frequency, contrary to what happens when a purely capacitive non dissipative electrical circuit is considered. In particular, the time domain governing equations of the in-plane free Bloch wave propagation turn out to be formally analogous to either those of a periodic viscoelastic continuum in the case of a dissipative electrical circuit, or analogous to those of a periodic elastic continuum in the case of a non dissipative electrical circuit. It follows that in the former case a complex-value frequency band structure is observed, while in the latter case a real-value one. Focus is on metamaterial shunted by electrical circuits characterized by equivalent purely capacitive admittance, in which the positive or negative-value capacitance can be externally modified. It follows that the changeable capacitance plays the role of a tuning parameter and is directly used to adaptively control the constitutive elastic properties of the piezoelectric shunting material, as well as, the resulting acoustic properties of the tunable metamaterial. In particular, attention is paid to tuning parameter ranges corresponding to positive values of the constitutive components of the elastic tensors. The influence of geometric design parameters on the Floquet–Bloch spectra of the acoustic metamaterials is investigated, as the tuning parameter changes. It is demonstrated that it is possible to open low-frequencies band gaps and controlling their amplitude and central frequencies by intervening on the tuning parameter, also starting from dense spectra. More specifically, by decreasing the tuning parameter up to about the *resonant* value, a stiffening of the piezoelectric material is observed, together with enlargements of low-frequency band gaps. Moreover, as expected the central frequencies of such band gaps tend to slightly increase. Finally, the effectiveness of the periodic tunable metamaterial as acoustic filter has been tested through a numerical experiment on a thin rectangular strip of homogeneous material in which a central strip has been replaced by a portion of the metamaterial. By imposing a mono-frequency time-harmonic displacement excitation to the left side of the specimen, it results that, as expected, when the excitation frequency falls into a pass band no filtering properties are exhibited. On the other hand, when the excitation frequency falls into a stop band, the tunable metamaterial behaves as a highly efficient acoustic filter. The promising results obtained can be positively exploited towards optimal design of tunable acoustic filters, adapt to a changing performance requirement in real-time.

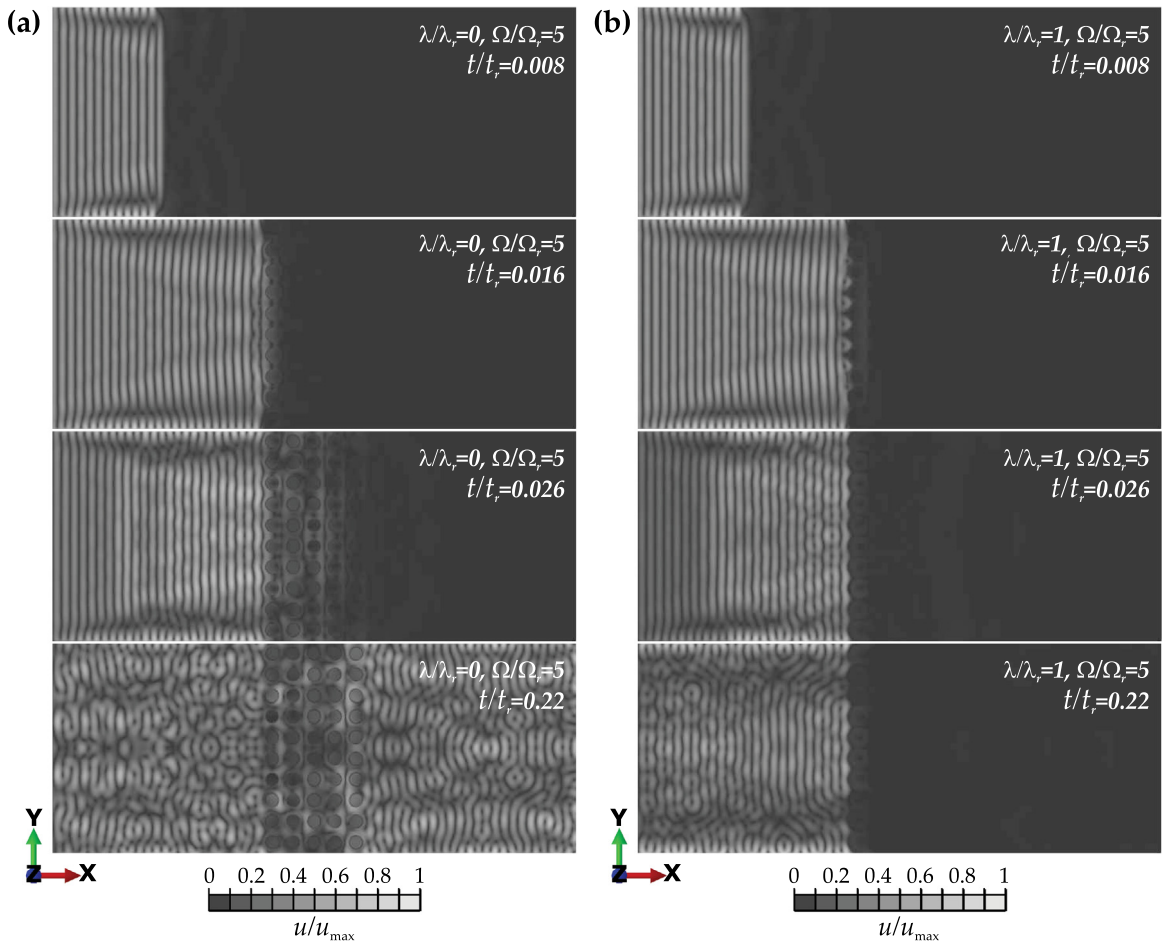

Fig. 15. Contour plots of the dimensionless displacement magnitudes u/u_{max} at different dimensionless time instants t/t_r for dimensionless excitation frequency $\Omega/\Omega_r = 5$. (a) $\lambda = 0$; (b) $\lambda \approx \lambda_R$.

Interesting future developments may concern, on the one hand, the study of the acoustic behaviour of tunable metamaterials connected to more sophisticated and even dissipative electrical circuits and, on the other, the design of tunable metamaterials with smart and/or imperfect microstructured interfaces [107–110].

Declaration of competing interest

The authors declare that they have no known competing financial interests or personal relationships that could have appeared to influence the work reported in this paper.

Acknowledgements

The authors acknowledge the financial support from National Group of Mathematical Physics (GNFM-INdAM), Italy. D.M is supported by the European Commission, Italy under the FET Open (Boheme) grant No. 863179.

Appendix A. Constitutive equations for the three-dimensional orthotropic piezoelectric material

The coupled constitutive relations for the three-dimensional orthotropic piezoelectric material with polarization along $\mathbf{e}_3$ in the stress–charge form read

$$\sigma_{ij} = C_{ijhk}\,\varepsilon_{hk} + C_{ij33}\,\varepsilon_{33} + e_{ij3}\,\frac{\partial\phi}{\partial x_3},$$
$$\sigma_{33} = C_{33hk}\,\varepsilon_{hk} + C_{3333}\,\varepsilon_{33} + e_{333}\,\frac{\partial\phi}{\partial x_3},$$
$$\sigma_{\alpha 3} = 2\,C_{\alpha 3\alpha 3}\,\varepsilon_{\alpha 3} + e_{\alpha 3\alpha}\,\frac{\partial\phi}{\partial x_l},$$
$$D_i = 2\,\widetilde{e}_{ij3}\,\varepsilon_{j3} + \beta_{ij}\,\frac{\partial\phi}{\partial x_j},$$
$$D_3 = \widetilde{e}_{3jh}\,\varepsilon_{jh} + \widetilde{e}_{333}\,\varepsilon_{33} - \beta_{33}\,\frac{\partial\phi}{\partial x_3}, \qquad i,j,h,k,\alpha = 1,2, \tag{21}$$

where from now on no summation on index α is applied, and being σ_{pq} the components of the stress tensor, D_p the components of the electric displacement field, $\varepsilon_{rs} = (\partial u_r/\partial x_s + \partial u_s/\partial x_r)/2$ is the components of the strain tensor, with u_p the displacement field components, ϕ the electric potential field, C_{pqrs} the components of the fourth order elasticity tensor, β_{pr} the components of the second order dielectric permittivity tensor, e_{qsp} the components of the third order piezoelectric stress–charge coupling tensor and its transpose $\widetilde{e}_{pqs} = e_{qsp}$.

For the sake of convenience we apply the bilateral Laplace transform to the governing Eqs. (21). By recalling the definition of the bilateral Laplace transform for a generic function $g(\mathbf{x}, t)$, i.e.

$$\mathcal{L}\,[g(\mathbf{x},t)] = \int_{-\infty}^{+\infty} g(\mathbf{x},t)e^{-st}dt = \widehat{g}(\mathbf{x},s), \tag{22}$$

being $s \in \mathbb{C}$ the Laplace variable playing the role of the complex angular frequency, the transformed coupled constitutive relations

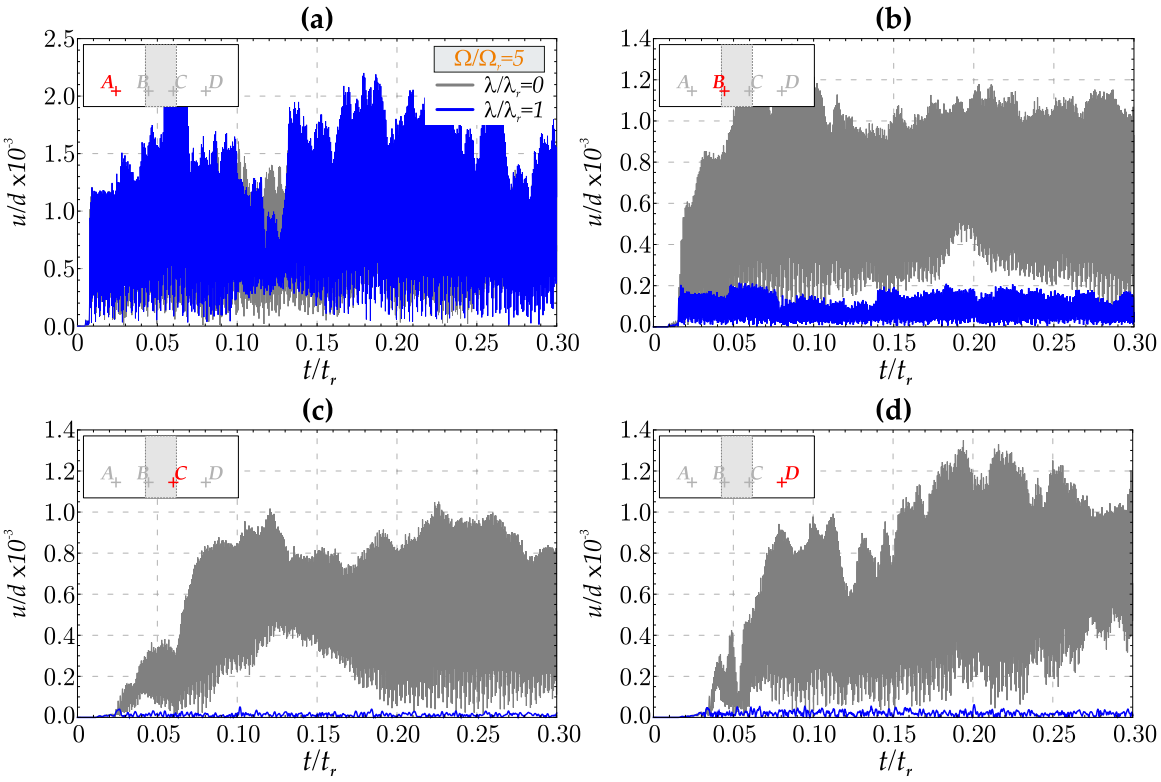

Fig. 16. Time histories of the dimensionless displacement magnitudes u/d versus the dimensionless time t/t_r for two characteristic values of the tuning parameter λ and for dimensionless excitation frequency $\Omega/\Omega_r = 5$ in four control points: (a) point A; (b) point B; (c) point C; (d) point D. (For interpretation of the references to colour in this figure legend, the reader is referred to the web version of this article.)

in the stress–charge form, read

$$\widehat{\sigma}_{ij} = C_{ijhk}\,\widehat{\varepsilon}_{hk} + C_{ij33}\,\widehat{\varepsilon}_{33} + e_{ij3}\,\frac{\partial\widehat{\phi}}{\partial x_3},$$
$$\widehat{\sigma}_{33} = C_{33hk}\,\widehat{\varepsilon}_{hk} + C_{3333}\,\widehat{\varepsilon}_{33} + e_{333}\,\frac{\partial\widehat{\phi}}{\partial x_3},$$
$$\widehat{\sigma}_{\alpha 3} = 2\,C_{\alpha 3\alpha 3}\,\widehat{\varepsilon}_{\alpha 3} + e_{\alpha 3\alpha}\,\frac{\partial\widehat{\phi}}{\partial x_\alpha},$$
$$\widehat{D}_i = 2\,\widetilde{e}_{ij3}\,\widehat{\varepsilon}_{j3} + \beta_{ij}\,\frac{\partial\widehat{\phi}}{\partial x_j},$$
$$\widehat{D}_3 = \widetilde{e}_{3jh}\,\widehat{\varepsilon}_{jh} + \widetilde{e}_{333}\,\widehat{\varepsilon}_{33} - \beta_{33}\,\frac{\partial\widehat{\phi}}{\partial x_3}, \qquad i,j,h,k,\alpha = 1,2. \tag{23}$$

The transformed electric potential difference $\widehat{V}_3$, imposed between the two opposite external surfaces of the piezoelectric ring, orthogonal to $\mathbf{e}_3$ as shown in Fig. 2(b), and the transformed current $\widehat{I}_3$ along the $\mathbf{e}_3$ direction are defined in the Laplace domain, in agreement with Hagood and von Flotow [76], as

$$\widehat{V}_3 = -L^{(P)}\frac{\partial\widehat{\phi}}{\partial x_3},$$
$$\widehat{I}_3 = s\,A^{(P)}\widehat{D}_3, \tag{24}$$

where $A^{(P)} = \pi((R - h/2)^2 - r^2)$ is the area of the piezoelectric annulus, and $L^{(P)} = w$. By replacing the Eqs. (24) into the constitutive relations (23), the transformed coupled constitutive relations (1), expressed in terms of $\widehat{V}_3$, $\widehat{I}_3$ are obtained.

Appendix B. Equivalent properties of the electrical circuit shunting the piezoelectric phase

Considering a generic external electrical circuit, the constitutive relations in terms of the electric potential difference $\widehat{V}_3$ and of the current $\widehat{I}_3$ in the transformed Laplace space result

$$\widehat{I}_3 = Y_{33}^{(SU)}(s)\,\widehat{V}_3. \tag{25}$$

where $Y_{33}^{(SU)}(s)$ is the equivalent admittance of the electrical circuit. By applying the inverse bilateral Laplace transform to (25), the following integral constitutive equation in the time domain is obtained

$$I_3 = \mathcal{L}^{-1}\left[\frac{Y_{33}^{(SU)}(s)}{s}\right] * \frac{\partial V_3}{\partial t}, \tag{26}$$

being $*$ is the convolution product. Note that Eq. (26) characterizes a generic non quasi-static electrical circuit (also referred as *time-modulated*) or an electric circuit with non purely capacitive equivalent admittance [111].

On the other hand, in the case of a purely capacitive equivalent admittance, i.e. when the equivalent admittance linearly depends on the Laplace variable s, the constitutive equation in the time domain takes the well-known form

$$I_3 = \mathcal{C}\delta(t) * \frac{\partial V_3}{\partial t} = \mathcal{C}\frac{\partial V_3}{\partial t}, \tag{27}$$

where $\delta(t)$ is the Dirac delta function.

Appendix C. Supplementary data

Supplementary material related to this article can be found online at https://doi.org/10.1016/j.eml.2020.100977.

References

[1] J.B. Pendry, Controlling electromagnetic fields, Science 312.5781 (2006) 1780–1782.
[2] D.R. Smith, W.J. Padilla, D.C. Vier, S.C. Nemat-Nasser, S. Schultz, Composite medium with simultaneously negative permeability and permittivity, Phys. Rev. Lett. 84 (2000) 4184–4187.

[3] R.W. Ziolkowski, E. Heyman, Wave propagation in media having negative permittivity and permeability, Phys. Rev. E 64 (5) (2001) 056625.
[4] Z. Liu, C.T. Chan, P. Sheng, Analytic model of phononic crystals with local resonances, Phys. Rev. B 71 (2005) 014103.
[5] N. Fang, D. Xi, J. Xu, M. Ambati, W. Srituravanich, C. Sun, X. Zhang, Ultrasonic metamaterials with negative modulus, Nature Mater. 5 (2006) 452–456.
[6] L.M. Magid, Mechanical energy flow in crystal lattices, Phys. Rev. 134 (1964) A158–A162.
[7] R.S. Langley, A transfer matrix analysis of the energetics of structural wave motion and harmonic vibration, Proc. R. Soc. Lond. Ser. A Math. Phys. Eng. Sci. 452 (1950) (1996) 1631–1648.
[8] M. Ostoja-Starzewski, Lattice models in micromechanics, Appl. Mech. Rev. 55 (1) (2002) 35–60.
[9] P. Martinsson, A.B. Movchan, Vibrations of lattice structures and phononic band gaps, Quart. J. Mech. Appl. Math. 56.1 (2003) 45–64.
[10] M. Ruzzene, F. Scarpa, F. Soranna, Wave beaming effects in two-dimensional cellular structures, Smart Mater. Struct. 12 (3) (2003) 363–372.
[11] K.F. Tee, A. Spadoni, F. Scarpa, M. Ruzzene, Wave propagation in auxetic tetrachiral honeycombs, J. Vib. Acoust. 132 (3) (2010) 031007.
[12] P.N. Demmie, M. Ostoja-Starzewski, Waves in fractal media, J. Elasticity 104 (1–2) (2011) 187–204.
[13] G. Allegri, F. Scarpa, R. Chowdhury, S. Adhikari, Wave propagation in periodically supported nanoribbons: A nonlocal elasticity approach, J. Vib. Acoust. 135 (4) (2013) 041017.
[14] F. Lemoult, N. Kaina, M. Fink, G. Lerosey, Wave propagation control at the deep subwavelength scale in metamaterials, Nat. Phys. 9 (1) (2013) 55.
[15] M. De Bellis, A. Bacigalupo, Auxetic behavior and acoustic properties of microstructured piezoelectric strain sensors, Smart Mater. Struct. 26 (8) (2017) 085037.
[16] A. Bacigalupo, L. Gambarotta, Dispersive wave propagation in two-dimensional rigid periodic blocky materials with elastic interfaces, J. Mech. Phys. Solids 102 (2017) 165–186.
[17] A. Bacigalupo, L. Gambarotta, Wave propagation in non-centrosymmetric beam-lattices with lumped masses: discrete and micropolar modeling, Int. J. Solids Struct. 118 (2017) 128–145.
[18] A. Piccolroaz, A. Movchan, L. Cabras, Dispersion degeneracies and standing modes in flexural waves supported by Rayleigh beam structures, Int. J. Solids Struct. 109 (2017) 152–165.
[19] A. Bacigalupo, M. Lepidi, Acoustic wave polarization and energy flow in periodic beam lattice materials, Int. J. Solids Struct. 147 (2018) 183–203.
[20] L. D'Alessandro, V. Zega, R. Ardito, A. Corigliano, 3D auxetic single material periodic structure with ultra-wide tunable bandgap, Sci. Rep. 8 (1) (2018) 2262.
[21] A. Bacigalupo, M.L. De Bellis, G. Gnecco, Complex frequency band structure of periodic thermo-diffusive materials by Floquet–Bloch theory, Acta Mech. 230 (9) (2019) 3339–3363.
[22] G. Bordiga, L. Cabras, D. Bigoni, A. Piccolroaz, Free and forced wave propagation in a Rayleigh-beam grid: Flat bands, Dirac cones, and vibration localization vs isotropization, Int. J. Solids Struct. 161 (2019) 64–81.
[23] F. Dal Corso, D. Tallarico, N.V. Movchan, A.B. Movchan, D. Bigoni, Nested bloch waves in elastic structures with configurational forces, Phil. Trans. R. Soc. A 377 (2156) (2019) 20190101.
[24] I.V. Kamotski, V.P. Smyshlyaev, Bandgaps in two-dimensional high-contrast periodic elastic beam lattice materials, J. Mech. Phys. Solids 123 (2019) 292–304, The N.A. Fleck 60th Anniversary Volume.
[25] H. Park, J. Oh, Study of abnormal group velocities in flexural metamaterials, Sci. Rep. 9 (2019) 13973.
[26] X. Guo, V.E. Gusev, V. Tournat, B. Deng, K. Bertoldi, Frequency-doubling effect in acoustic reflection by a nonlinear, architected rotating-square metasurface, Phys. Rev. E 99 (5) (2019) 052209.
[27] A. Bacigalupo, L. Gambarotta, Chiral two-dimensional periodic blocky materials with elastic interfaces: Auxetic and acoustic properties, Extreme Mech. Lett. (2020) 100769.
[28] M.-H. Lu, L. Feng, Y.-F. Chen, Phononic crystals and acoustic metamaterials, Mater. Today 12 (12) (2009) 34–42.
[29] J. Liu, H. Guo, T. Wang, A review of acoustic metamaterials and phononic crystals, Crystals 10 (4) (2020) 305.
[30] A. Diaz, A. Haddow, L. Ma, Design of band-gap grid structures, Struct. Multidiscip. Optim. 29 (6) (2005) 418–431.
[31] A. Bacigalupo, M. Lepidi, G. Gnecco, L. Gambarotta, Optimal design of auxetic hexachiral metamaterials with local resonators, Smart Mater. Struct. 25 (5) (2016) 054009.
[32] M. Ranjbar, L. Boldrin, F. Scarpa, S. Neild, S. Patsias, Vibroacoustic optimization of anti-tetrachiral and auxetic hexagonal sandwich panels with gradient geometry, Smart Mater. Struct. 25 (5) (2016) 054012.
[33] Z.P. Wang, L.H. Poh, J. Dirrenberger, Y. Zhu, S. Forest, Isogeometric shape optimization of smoothed petal auxetic structures via computational periodic homogenization, Comput. Methods Appl. Mech. Engrg. 323 (2017) 250–271.
[34] A. Bacigalupo, G. Gnecco, M. Lepidi, L. Gambarotta, Machine-learning techniques for the optimal design of acoustic metamaterials, J. Optim. Theory Appl. (2019) http://dx.doi.org/10.1007/s10957-019-01614-8.
[35] M. Bruggi, A. Corigliano, Optimal 2D auxetic micro-structures with band gap, Meccanica 54 (13) (2019) 2001–2027.
[36] M. Choi, M. Oh, B. Koo, S. Cho, Optimal design of lattice structures for controllable extremal band gaps, Sci. Rep. 9 (1) (2019) 1–13.
[37] D. Kumar, Z. Wang, L.H. Poh, S.T. Quek, Isogeometric shape optimization of smoothed petal auxetics with prescribed nonlinear deformation, Comput. Methods Appl. Mech. Engrg. 356 (2019) 16–43.
[38] J. Rong, W. Ye, Topology optimization design scheme for broadband non-resonant hyperbolic elastic metamaterials, Comput. Methods Appl. Mech. Engrg. 344 (2019) 819–836.
[39] X.N. Liu, G.K. Hu, C.T. Sun, G.L. Huang, Wave propagation characterization and design of two-dimensional elastic chiral metacomposite, J. Sound Vib. 330 (11) (2011) 2536–2553.
[40] J. Christensen, F.J. García de Abajo, Negative refraction and backward waves in layered acoustic metamaterials, Phys. Rev. B 86 (2012) 024301.
[41] L. Morini, Y. Eyzat, M. Gei, Negative refraction in quasicrystalline multilayered metamaterials, J. Mech. Phys. Solids 124 (2019) 282–298.
[42] G. Bordiga, L. Cabras, A. Piccolroaz, D. Bigoni, Prestress tuning of negative refraction and wave channeling from flexural sources, Appl. Phys. Lett. 114 (2019) 041901.
[43] X. Yan, R. Zhu, G. Huang, F.G. Yuan, Focusing guided waves using surface bonded elastic metamaterials, Appl. Phys. Lett. 103 (12) (2013) 121901.
[44] J. Park, C. Park, K. Lee, S. Lee, Acoustic superlens using membrane-based metamaterials, Appl. Phys. Lett. 106(5) (2015) 051901.
[45] B. Brun, N. Moreau, S. Somanchi, V.H. Nguyen, K. Watanabe, T. Taniguchi, J. Charlier, C. Stampfer, B. Hackens, Imaging Dirac fermions flow through a circular Veselago lens, Phys. Rev. B 100 (2019) 041401(R).
[46] M. Brun, S. Guenneau, A.B. Movchan, Achieving control of in-plane elastic waves, Appl. Phys. Lett. 94 (2009) 061903.
[47] A.N. Norris, A.L. Shuvalov, Elastic cloaking theory, Wave Motion 48 (2011) 525–538.
[48] D. Colquitt, M. Brun, M. Gei, A. Movchan, N. Movchan, I. Jones, Transformation elastodynamics and cloaking for flexural waves, J. Mech. Phys. Solids 72 (2014) 131–143.
[49] D. Misseroni, D. Colquitt, A. Movchan, N. Movchan, I. Jones, Cymatics for the cloaking of flexural vibrations in a structured plate, Sci. Rep. 6 (2016) 23929.
[50] N. Stenger, M. Wilhelm, M. Wegener, Experiments on elastic cloaking in thin plates, Phys. Rev. Lett. 108 (1) (2012) 014301.
[51] M. Brun, G.F. Giaccu, A.B. Movchan, N.V. Movchan, Asymptotics of eigenfrequencies in the dynamic response of elongated multi-structures, Proc. R. Soc. Lond. Ser. A Math. Phys. Eng. Sci. 468 (2138) (2012) 378–394.
[52] M. Brun, A.B. Movchan, I.S. Jones, Phononic band gap systems in structural mechanics: finite slender elastic structures and infinite periodic waveguides, J. Vib. Acoust. 135 (4) (2013) 041013.
[53] S. Brûlé, E. Javelaud, S. Enoch, S. Guenneau, Experiments on seismic metamaterials: Molding surface waves, Phys. Rev. Lett. 112 (2014) 133901.
[54] Y. Achaoui, B. Ungureanu, S. Enoch, S. Brûlé, S. Guenneau, Seismic waves damping with arrays of inertial resonators, Extreme Mech. Lett. 8 (2016) 30–37, Nanomechanics: Bridging Spatial and Temporal Scales.
[55] Y. Achaoui, T. Antonakakis, S. Brûlé, R.V. Craster, S. Enoch, S. Guenneau, Clamped seismic metamaterials: ultra-low frequency stop bands, New J. Phys. 19 (6) (2017) 063022.
[56] G. Carta, A.B. Movchan, L.P. Argani, O.S. Bursi, Quasi-periodicity and multi-scale resonators for the reduction of seismic vibrations in fluid-solid systems, Internat. J. Engrg. Sci. 109 (2016) 216–239.
[57] A. Colombi, D. Colquitt, P. Roux, S. Guenneau, R.V. Craster, A seismic metamaterial: The resonant metawedge, Sci. Rep. 6 (2016) 27717.
[58] M. Miniaci, A. Krushynska, F.B.N. Pugno, Large scale mechanical metamaterials as seismic shields, New J. Phys. 18 (2016) 083041.
[59] R. Craster, A. Colombi, P. Roux, Elastic metamaterials applied to geophysics, Impact 2018 (5) (2018) 68–70.
[60] B. Ungureanu, S. Guenneau, Y. Achaoui, A. Diatta, M. Farhat, H. Hutridurga, R.V. Craster, S. Enoch, S. Brûlé, The influence of building interactions on seismic and elastic body waves, EPJ Appl. Metamaterials 6 (2019) 18.
[61] W.J. Parnell, Nonlinear pre-stress for cloaking from antiplane elastic waves, Proc. R. Soc. Lond. Ser. A Math. Phys. Eng. Sci. 468 (2138) (2011) 563–580.
[62] M. Kadic, T. Bückmann, R. Schittny, P. Gumbsch, M. Wegener, Pentamode metamaterials with independently tailored bulk modulus and mass density, Phys. Rev. A 2 (5) (2014) 054007.
[63] L. Zigoneanu, B.I. Popa, S.A. Cummer, Three-dimensional broadband omnidirectional acoustic ground cloak, Nature Mater. 13 (4) (2014) 352.

[64] A. Darabi, A. Zareei, M. Alam, M.J. Leamy, Experimental demonstration of an ultrabroadband nonlinear cloak for flexural waves, Phys. Rev. Lett. 121 (17) (2018) 174301.
[65] D. Misseroni, A. Movchan, D. Bigoni, Omnidirectional flexural invisibility of multiple interacting voids in vibrating elastic plates, Proc. R. Soc. Lond. Ser. A Math. Phys. Eng. Sci. 475 (2019) 2229.
[66] X.N. Liu, G.K. Hu, G.L. Huang, C.T. Sun, An elastic metamaterial with simultaneously negative mass density and bulk modulus, Appl. Phys. Lett. 98 (25) (2011) 251907.
[67] X. Zhou, X. Liu, G. Hu, Elastic metamaterials with local resonances: an overview, Theor. Appl. Mech. Lett. 4 (2012) 041001.
[68] D. Bigoni, S. Guenneau, A. Movchan, M. Brun, Elastic metamaterials with inertial locally resonant structures: Application to lensing and localization, Phys. Rev. B 87(17) (2013) 174303.
[69] A. Bacigalupo, L. Gambarotta, Simplified modelling of chiral lattice materials with local resonators, Int. J. Solids Struct. 83 (2016) 126–141.
[70] S.A. Cummer, J. Christensen, A. Alù, Controlling sound with acoustic metamaterials, Nature Rev. Mater. 1.3 (2016) 16001.
[71] G. Ma, P. Sheng, Acoustic metamaterials: From local resonances to broad horizons, Sci. Adv. 2 (2) (2016).
[72] X. Zhou, J. Wang, R. Wang, J. Lin, Effects of relevant parameters on the bandgaps of acoustic metamaterials with multi-resonators, Appl. Phys. A 122 (2016) 427.
[73] N. Kaina, A. Causier, Y. Bourlier, M. Fink, T. Berthelot, G. Lerosey, Slow waves in locally resonant metamaterials line defect waveguides, Sci. Rep. 7 (1) (2017) 15105.
[74] M. Lepidi, A. Bacigalupo, Multi-parametric sensitivity analysis of the band structure for tetrachiral acoustic metamaterials, Int. J. Solids Struct. 136–137 (2018) 186–202.
[75] R.L. Forward, Electronic damping of vibrations in optical structures, Appl. Opt. 18 (1979) 690–697.
[76] N. Hagood, A. von Flotow, Damping of structural vibrations with piezoelectric materials and passive electrical networks, J. Sound Vib. 146 (2) (1991) 243–268.
[77] J.J. Hollkamp, Multimodal passive vibration suppression with piezoelectric materials and resonant shunts, J. Intell. Mater. Syst. Struct. 5(1) (1994) 49–57.
[78] A. Preumont, Vibration Control of Active Structures, volume 2, Springer, 1997.
[79] O. Thomas, J. Deü, J. Ducarne, Vibrations of an elastic structure with shunted piezoelectric patches: efficient finite element formulation an electromechanical coupling coefficients, Internat. J. Numer. Methods Engrg. 80 (2009) 235–268.
[80] G. Wang, J. Wang, S. Chen, J. Wen, Vibration attenuations induced by periodic arrays of piezoelectric patches connected by enhanced resonant shunting circuits, Smart Mater. Struct. 20 (12) (2011) 125019.
[81] A. Bergamini, T. Delpero, L.D. Simoni, L.D. Lillo, M. Ruzzene, P. Ermanni, Phononic crystal with adaptive connectivity, Adv. Mater. 26 (9) (2014) 1343–1347.
[82] H. Zhang, J. Wen, Y. Xiao, G. Wang, X. Wen, Sound transmission loss of metamaterial thin plates with periodic subwavelength arrays of shunted piezoelectric patches, J. Sound Vib. 343 (2015) 104–120.
[83] X. Li, Y. Chen, G. Hu, G. Huang, A self-adaptive metamaterial beam with digitally controlled resonators for subwavelength broadband flexural wave attenuation, Smart Mater. Struct. 27 (4) (2018) 045015.
[84] S. Chen, Y. Fan, Q. Fu, H. Wu, Y. Jin, J. Zheng, F. Zhang, A review of tunable acoustic metamaterials, Appl. Sci. 8 (9) (2018) 1480.
[85] K. Marakakis, G.K. Tairidis, P. Koutsianitis, G.E. Stavroulakis, Shunt piezoelectric systems for noise and vibration control: A review, Front. Built Environ. 5 (2019) 64.
[86] F. Zangeneh-Nejad, R. Fleury, Active times for acoustic metamaterials, Rev. Phys. 4 (2019) 100031.
[87] O. Thorp, M. Ruzzene, A. Baz, Attenuation and localization of wave propagation in rods with periodic shunted piezoelectric patches, Smart Mater. Struct. 10 (5) (2001) 979.
[88] L. Airoldi, M. Ruzzene, Design of tunable acoustic metamaterials through periodic arrays of resonant shunted piezos, New J. Phys. 13 (11) (2011) 113010.
[89] F. Casadei, T. Delpero, A. Bergamini, P. Ermanni, M. Ruzzene, Piezoelectric resonator arrays for tunable acoustic waveguides and metamaterials, J. Appl. Phys. 112 (6) (2012) 064902.
[90] M. Collet, M. Ouisse, M.N. Ichchou, Structural energy flow optimization through adaptive shunted piezoelectric metacomposites, J. Intell. Mater. Syst. Struct. 23 (15) (2012) 1661–1677.
[91] B.S. Beck, K.A. Cunefare, M. Collet, The power output and efficiency of a negative capacitance shunt for vibration control of a flexural system, Smart Mater. Struct. 22 (6) (2013) 065009.
[92] B.S. Beck, K.A. Cunefare, M. Collet, Response-based tuning of a negative capacitance shunt for vibration control, J. Intell. Mater. Syst. Struct. 25 (13) (2014) 1585–1595.
[93] Y. Chen, G. Hu, G. Huang, An adaptive metamaterial beam with hybrid shunting circuits for extremely broadband control of flexural waves, Smart Mater. Struct. 25 (10) (2016) 105036.
[94] M. Ouisse, M. Collet, F. Scarpa, A piezo-shunted kirigami auxetic lattice for adaptive elastic wave filtering, Smart Mater. Struct. 25 (11) (2016) 115016.
[95] R. Zhu, Y.Y. Chen, M.V. Barnhart, G.K. Hu, C.T. Sun, G.L. Huang, Experimental study of an adaptive elastic metamaterial controlled by electric circuits, Appl. Phys. Lett. 108 (1) (2016) 011905.
[96] J. Xu, R. Yan, J. Tang, Broadening bandgap width of piezoelectric metamaterial by introducing cavity, Appl. Sci. 8(9) (2018) 1606.
[97] G. Li, Y. Wang, Y. Wang, Active control on switchable waveguide of elastic wave metamaterials with the 3D printing technology, Sci. Rep. 9 (1) (2019) 1–8.
[98] R. Toupin, Stress tensors in elastic dielectrics, Arch. Ration. Mech. Anal. 5 (1960) 440.
[99] J.R. Westra, C.J. Verhoeven, A.H. Van Roermund, Oscillators and Oscillator Systems, Springer, 2000.
[100] G. Floquet, Sur les équations différentielles linéaires à coefficients périodiques, Ann. Éc. Norm. Supér. 12 (1883) 47–88.
[101] F. Bloch, Uber die quantenmechanik der Elektronen in Kristallgittern, Z. Phys. 52 (1928) 555–600.
[102] L. Brillouin, Wave Propagation and Group Velocity, Academic Press, New York, 1960.
[103] H.J. Lee, S. Zhang, Y. Bar-Cohen, S. Sherrit, High temperature, high power piezoelectric composite transducers, Sensors 14 (8) (2014) 14526–14552.
[104] S. Iyer, T. Venkatesh, Electromechanical response of (3–0, 3–1) particulate, fibrous, and porous piezoelectric composites with anisotropic constituents: A model based on the homogenization method, Int. J. Solids Struct. 51 (6) (2014) 1221–1234.
[105] R. Courant, K. Friedrichs, H. Lewy, On the partial difference equations of mathematical physics, IBM J. Res. Dev. 11 (2) (1967) 215–234.
[106] C.A. De Moura, C.S. Kubrusly, The Courant–Friedrichs–Lewy (CFL) Condition, Springer, 2013.
[107] Y. Zhou, C. Lü, W. Chen, Bulk wave propagation in layered piezomagnetic/piezoelectric plates with initial stresses or interface imperfections, Compos. Struct. 94 (9) (2012) 2736–2745.
[108] I. Sevostianov, R. Rodriguez-Ramos, R. Guinovart-Diaz, J. Bravo-Castillero, F. Sabina, Connections between different models describing imperfect interfaces in periodic fiber-reinforced composites, Int. J. Solids Struct. 49 (13) (2012) 1518–1525.
[109] R. Massabò, I. Monetto, Local zigzag effects and brittle delamination fracture of n-layered beams using a structural theory with three displacement variables, Frat. Integrità Strutt. 14 (51) (2020) 275–287.
[110] I. Monetto, The effects of an interlayer debond on the flexural behavior of three-layer beams, Coatings 9 (4) (2019) 258.
[111] R. Robert, S.M. Berleze, Integro-differential equation of absorptive capacitors, IEEE Trans. Dielectr. Electr. Insul. 8 (2) (2001) 244–247.